Argon Diffusion Gradients in Micas and Implications for the Thermal History of the Sandia Pluton

by

Ellen A. Dotson

B.S., Earth, Atmospheric and Planetary Sciences
Massachusetts Institute of Technology, 1993

Submitted to the Department of Earth, Atmospheric, and Planetary Sciences in Partial Fulfillment of the Requirements for the Degree of

Master of Science

at the
Massachusetts Institute of Technology

August 1994

Signature of Author _____
Department of Earth, Atmospheric, and Planetary Sciences
August, 1994

Certified by_____
Professor Kip V. Hodges
Thesis Supervisor

Accepted by_____
Thomas H. Jordan
Department Head

Argon Diffusion Gradients in Micas and Implications for the Thermal History of the Sandia Pluton

by

Ellen A. Dotson

Submitted to the Department of Earth, Atmospheric, and Planetary Sciences
on August 23, 1994 in partial fulfillment of the requirements for the
Degree of Master of Science in
Earth, Atmospheric, and Planetary Sciences

Abstract

Micas from slowly cooled terranes can contain significant age gradients produced by thermally-activated diffusion of argon. Previously published work (Dodson, 1986) has shown that the distribution of apparent ages in such samples can yield important thermal history information, but the method used was predicated on the assumption that T^{-1} increased linearly with time. Using a finite difference approximation of the diffusion equation to simulate argon gradients for an assortment of slow-cooling T-t paths, I show that Dodson's (1986) equation predicts closure temperature profiles and integrated cooling rates over the closure interval with reasonable accuracy regardless of the functional form of the T-t curve. Because closure intervals can vary greatly as a function of composition and size, a collection of diverse micas with age gradients from a slowly cooled terrane can define a cooling path with great detail. The usefulness of this approach is illustrated with a suite of micas from the Sandia pluton, a ~ 1.45 Ga anorogenic granite in central New Mexico. $^{40}Ar/^{39}Ar$ laser microprobe analyses indicated apparent age gradients that exhibit ranges up to 450 Ma in age in an individual crystal. The integrated cooling rates obtained from these micas, define a cooling history which suggests a transient thermal pulse related to emplacement of the pluton, followed by a remarkably stable, protracted (> 500 Ma) slow cooling (<< 1 K/Ma).

Thesis Advisor: Kip V. Hodges, Professor of Geology

Acknowledgments

I would like to thank Kip Hodges for his insight, guidance, humor, and considerable patience as an editor, without which this thesis would never have seen the light of day.

My friend Nicholas Roosevelt has my deep gratitude for his steadfast faith and patience throughout this year. He is the best of companions.

My deepest gratitude goes to my parents, Margaret and Adrian Dotson, whose steady love and support has been, and always will be, the most valuable of gifts.

Table of Contents

Chapter 1

Introduction

In order to understand cooling histories of geologic materials, geochronologists rely on several assumptions regarding the diffusion of radiogenic daughter isotopes out of mineral systems. Thermally-activated diffusion is thought to be a primary mechanism for the loss of daughter isotopes. To relate apparent age to the cooling history of a sample, geochronologists rely on a mathematical equations (Dodson, 1973; Dodson, 1986) derived from a solution to the diffusion equation. The validity of these equations depends on a number of assumptions being correct: the mineral is assumed to be initially in equilibrium with its environment; the diffusion parameters for various mineral systems must be known; and this solution is exactly true only when T^{-1} increases linearly with time. In order to test the reliability of Dodson's equations for samples which experience cooling histories that are not linear with T^{-1}, a numerical finite difference approximation of the diffusion equation was utilized to model argon gradients for a variety of cooling histories. These results were then compared to the predictions made by Dodson's solution.

1.1 Diffusion

Diffusion is the mechanism by which molecules are transported through some medium by the random molecular motions. Imagine a system with a finite amount of diffusing component X, which initially has a high-concentration region (region A) with a concentration of X_A, and a low-concentration region (region B) with concentration X_B. For any individual

diffusing component in the system, each motion step is entirely random. An individual X has an equal probability of moving either towards or away from region A during any single step. At any one instant, a constant percentage of the total number of X is moving away from A and toward B. An equal percentage is moving towards A and away from B. Now imagine a plane which separates A and B. A constant percentage of X_A, crosses the boundary into region B, while an equal percentage of X_B, crosses the boundary into region A. But, because there is a higher absolute number of X in region A, there will be a net transport of X from A into B until, over time, both sides have the same concentration of X. The system is then said to be in equilibrium with respect to X (cg. Crank, 1975; Shewmon,1989)

In geochronological systems, the diffusing component of interest is the daughter product of some radioactive parent isotope with a known half-life. Initially upon crystallization, a mineral will be at isotopic equilibrium with its surrounding environment with respect to the daughter product. The ambient concentration of the daughter product is incorporated into the crystal structure. In the case of thermally-activated diffusion, as the mineral cools and the daughter product is being produced by radioactive decay, the daughter product will take random steps with a lower frequency and the crystal lattice will become more "rigid". This process makes it more difficult for the daughter product to move from place to place within the crystal. If the concentration of the daughter product is higher within the mineral than in its surrounding environment, equilibrium requires the daughter product to diffuse out of the mineral. As a mineral cools, the daughter product diffuses less rapidly out of the mineral system. When the production rate is greater than the loss due to diffusion, the mineral system retains some portion of the daughter product, and the system is out of equilibrium with its surrounding environment. The

diffusivity of a system can be qualitatively thought of as a measure of the ease with which a particular diffusing component can move through a particular medium, given a certain set of conditions, such as temperature, pressure, chemical composition of the mineral and quantity of vacancies within the medium.

1.2 $^{40}Ar/^{39}Ar$ Thermochronology

Traditional $^{40}Ar/^{39}Ar$ thermochronologic studies utilize the varying thermal diffusivities of argon in different minerals to constrain the temperature-time history of a sample. The fundamental assumption of this approach is that the primary argon-loss mechanism is thermally activated diffusion of the sort described above. For thermally activated diffusion, D, the diffusivity, follows an Arrhenius relationship,

$$D = D_0 \exp\left[-\frac{E}{RT}\right] \tag{1}$$

where E is the activation energy, R is the universal gas constant, T is temperature and D_0 is the diffusivity at infinite temperature. It can be observed from this relationship that D is strongly dependent upon the temperature of the system. Above some critical temperature range the mineral loses virtually all of the radiogenic argon as it is being produced; below this critical temperature range, essentially, all of the radiogenic argon produced in a mineral is retained. The rate at which a sample cools through this transitional temperature range has a profound effect upon argon retention, and subsequently, on the extent of time-temperature information which can be gathered from a sample.

For example, if a specimen undergoes rapid cooling, as it would in a volcanic or hypabyssal setting, the sample rapidly traverses the transitional temperature ranges of the K-rich minerals. The apparent $^{40}Ar/^{39}Ar$ ages of assorted K-rich minerals from a single sample will be virtually identical to one another and to the crystallization age of the mineral.

In contrast, when a sample undergoes moderate cooling, different K-rich minerals from the same specimen will exhibit significantly disparate apparent $^{40}Ar/^{39}Ar$ ages due to the differing diffusivities of argon in different mineral systems.

Dodson (1973), presented an equation derived from a solution to the diffusion equation;

$$T_c = R \Big/ \left[E \ln\left(A \tau D_o / a^2 \right) \right] \qquad (2)$$

which gives the integrated closure temperature as a function of E, D_O, A (a constant depending on diffusion geometry of the mineral and the radioactive decay rate), a (the characteristic diffusion radius of a particular mineral), and τ (the time constant). τ, the time constant is defined as,

$$\tau = - R T^2 \Big/ \left(E \, dT/dt \right) \qquad (3)$$

Equation (2) is exactly true only when T^{-1} increases linearly with time. The integrated apparent $^{40}Ar/^{39}Ar$ age records the time at which a particular mineral passes through the closure temperature predicted by this equation. By applying this method to a variety of K-rich minerals from a geographic region, one can constrain the temperature-time history of a tectonic region.

When a mineral experiences slow cooling through its transitional temperature range, a measurable concentration gradient of the diffusing

component will be developed within the mineral grain. This occurs because as the sample cools, the mean distance the diffusing substance will travel during a unit time decreases (Shewmon, 1989). A daughter product originating in the center of the grain must travel a greater distance to reach the free surface at the grain boundary, and thus has a smaller probability of escaping the system. The mean distance traveled in a unit time decreases as the system cools, while the production rate remains constant. The center of the mineral begins to retain radiogenic argon, while daughter product in the outer portion of the grain remains in equilibrium with the environment. Over time, a concentric gradient, with higher concentrations in the center and lower concentrations near the edge, will be developed as the system passes through the transitional temperature range. This gradient should be measurable when the time taken to traverse the critical temperature range is longer than the experimental uncertainty associated with the $^{40}Ar/^{39}Ar$ dating technique.

Dodson (1986) presented the following equation which predicts the spatial distribution of closure temperatures for samples which have undergone slow cooling.

$$E/RT_c = G(x) + \ln\left(\tau D_o / a^2\right) \qquad (4)$$

G(x) is a geometric term which depends upon the diffusion geometry of the mineral and the position x within the mineral, and a is the grain radius. Once again, this equation is exactly true only when T^{-1} increases linearly with time. This equation provides a way to constrain a portion of the temperature-time path by analyzing the radiogenic argon gradients within a single mineral grain.

In recent work by Hames and Hodges (1993) and Hodges et al. (1994), significant age gradients were measured in individual muscovite and biotite and biotite grains. In the study by Hodges et al. (1994), individual muscovite and biotite grains from the Crazy Basin monzogranite from central Arizona were analyzed. Spot fusion mapping of the {001} cleavage plane using a focused 10W-Ar laser revealed broadly concentric age gradients from 1650 ma to 1270 Ma in the muscovite sample, and from 1420 Ma to 1150 Ma in the biotite sample. Assuming that these gradients were developed by thermally activated diffusion, they utilized equation (4), to obtain an integrated cooling rate of -0.30 K/m.y. through the transitional temperature range for the muscovite, and a cooling rate of -0.33 K/m.y. for the biotite. They argued that the agreement between these results provides persuasive evidence for very slow cooling of the Crazy Basin monzogranite.

There is no geological reason to justify an a priori assumption that all regions which undergo slow cooling follow a cooling path in which T^{-1} increases linearly with time. The question arises, what would be the morphology of diffusion gradients in minerals which undergo slow cooling along other cooling paths? Do these gradients differ significantly from gradients formed by linear T^{-1} cooling? Given these gradients, if one applies Dodson's 1986 method, how well does his integrated cooling rate approximate the different cooling rates through the transitional temperature range? The second chapter of this thesis attempts to answer these questions, by forward modeling diffusion gradients for a variety of cooling curves that are not linear with T^{-1} using finite difference techniques, and the then comparing these to Dodson's (1986) model.

As will be shown in chapter 2, equation (4) does a good job of predicting the closure temperatures and cooling rates based on gradients developed by slow cooling paths not necessarily linear with T^{-1}. It is possible to define a portion of a cooling curve that is not linear with T^{-1}, by using equation (4), with gradients developed in a number of minerals of different sizes and compositions. The size and composition of a mineral has a profound effect on the transitional temperature range, and thus records different portions of the cooling history. The third chapter presents argon microprobe data from a suite of micas from the Sandia pluton in New Mexico. The cooling rates predicted by equation (4) for these micas collectively form a coherent cooling curve that is not linear with T^{-1}. These results suggest that it is possible to define detailed cooling histories in slowly cooled terranes by analysis of argon gradients for a suite of samples.

Chapter 2

Modeling Volume Diffusion of Argon in Biotite

2.1 Introduction

A number of recent studies (Hames and Hodges, 1993; Hodges et al, 1994) have mapped out argon gradients on individual mica grains. These gradients were interpreted to be diffusion gradients formed by thermally-activated diffusion. The gradients were broadly concentric, with older ages at the center, and younger ages at the rim. This age profile, if developed by thermally activated diffusion, indicates that the effective diffusion radius of mica is the size of the grain. The age gradients were used to calculate cooling rates by applying Dodson's (1986) equation relating closure temperature and cooling rate to age and position.

Dodson's (1986) equation is exactly true only when T^{-1} increases linearly with time, and therefore we must ask ourselves how well does equation (4) predict cooling rates when T^{-1} is not linear with time. This study focuses on the application of finite difference analytical methods to predict the morphology of argon gradients in biotite developed by thermally activated diffusion. This approach easily allows one to predict argon gradients for a variety of cooling rates and initial argon gradients. The morphology of argon gradients in biotite is forward modeled for a variety of temperature-time paths. The predicted concentration gradients are then converted to age gradients and closure temperature profiles. The modeled gradients are compared with Dodson's predicted gradients to gain insight into the robustness of his method.

2.2 The Diffusion Equations

In 1855 Aldof Fick set forth the fundamental equations describing the process of diffusion. He recognized that the process of material diffusing through a medium was parallel to the diffusion of thermal energy through a system, and adapted Fourier's Law of Heat Conduction to the diffusion of material. Fick's first law states the flux of material through an area is proportional to the concentration gradient. Specifically,

$$J = -D\frac{\partial C}{\partial x}, \tag{5}$$

where J is the rate of transfer of material through a unit area, C is the concentration of the diffusion material and D is the diffusion coefficient for the system. The negative sign indicates that flux occurs in the direction opposite that of increasing concentration. It is important to note that D is independent of the concentration gradient (Shewmon, 1989).

The derivation of Fick's second law follows easily from Fick's first law (Crank,1975). Suppose we have a rectangular parallelepiped whose center is at point (x,y,z) and the length of the edges are 2dx, 2dy, and 2dz.

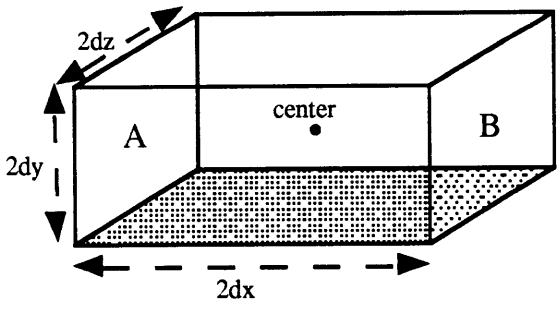

Suppose we have some substance diffusing either into or out of our system. The rate at which the diffusing substance enters or leaves the system is equal to

the change in concentration (i.e. amount per unit volume) per unit time, multiplied by the volume of the object of interest, explicitly,

$$8dxdydz\frac{\partial C}{\partial t}, \tag{6}$$

where t is time. The rate at which the diffusing substance enters or leaves the system can also be expressed as the sum of flux through each surface bounding the system. For plane A, which is normal to the x axis passing through point x - dx, the rate of material entering the system through this plane is equal to

$$4dydz\left(J_x - \frac{\partial J_x}{\partial x}dx\right), \tag{7}$$

where J_X is the flux through a plane normal through the x axis passing through center point (x,y,z). Similarly the rate of material leaving the system through plane B, which is normal to the x axis passing through point x + dx, is equal to

$$4dydz\left(J_x + \frac{\partial J_x}{\partial x}dx\right). \tag{8}$$

Thus, the rate of increase of the diffusing substance in the system due to flux across these two planes is

$$-8dxdydz\frac{\partial J_x}{\partial x}. \tag{9}$$

Similarly, the rate of increase due to flux across boundaries normal to the y axis and z axis is equal to

$$-8dxdydz\frac{\partial J_y}{\partial y} \text{ and } -8dxdydz\frac{\partial J_z}{\partial z} \text{ respectively.} \tag{10}$$

If we assume that the production of the diffusing substance within the system is equal to zero then,

$$\frac{\partial C}{\partial t}+\frac{\partial J_x}{\partial x}+\frac{\partial J_y}{\partial y}+\frac{\partial J_z}{\partial z}=0. \qquad (11)$$

If diffusion is isotropic, i.e. occurs equally in all directions, and is constant, then,

$$\frac{\partial C}{\partial t}=D\left(\frac{\partial^2 C}{\partial x^2}+\frac{\partial^2 C}{\partial y^2}+\frac{\partial^2 C}{\partial z^2}\right). \qquad (12)$$

This equation is known as Fick's second Law. The diffusion of argon in biotite is commonly thought to be cylindrical in geometry (Giletti, 1974; Harrison et al, 1985). This equation can be transformed into cylindrical coordinates by substituting,

$$x = r\cos\theta \text{ and } y = r\sin\theta.$$

Giving,

$$\frac{\partial C}{\partial t}=\frac{1}{r}\left\{\frac{\partial}{\partial r}\left(rD\frac{\partial C}{\partial r}\right)+\frac{\partial}{\partial \theta}\left(\frac{D}{r}\frac{\partial C}{\partial \theta}\right)+\frac{\partial}{\partial z}\left(rD\frac{\partial C}{\partial z}\right)\right\}, \qquad (13)$$

with cylindrical coordinates r, θ, z.

2.3 Requirements of Geologically Useful Solutions to the Diffusion Equation

A geologically useful solution to the diffusion equation will include a radiogenic production term for the diffusing substance of interest, and will also take into account the time variance of D, the diffusivity coefficient. Dodson's 1973 solution to the diffusion equation fulfills these requirements, and it's applicability and usefulness will be discussed below.

The loss of argon in biotite is thought to be due to thermally activated diffusion. When the temperature of the system changes with time, D varies with time. In order to solve the diffusion equation in this situation, a new time scale is introduced.

D is taken to be some $f(t)$; the new time scale, τ, is defined such that,

$$d\tau = f(t)\, dt. \tag{14}$$

Fick's second law becomes,

$$\frac{\partial C}{\partial \tau} = \frac{\partial^2 C}{\partial x^2} + \frac{\partial^2 C}{\partial y^2} + \frac{\partial^2 C}{\partial z^2}. \tag{15}$$

Mathematical solutions for such diffusion equations are exactly true only for the temperature-time path defined by $f(t)$.

In Dodson's (1973) paper, he presented a solution which defined the time scale τ (equation 3), as the time constant for which D decreases by a factor of e^{-1}, when T^{-1} increases linearly with time. The solution for mean closure temperature (equation 2), requires the assumption that the mineral starts out with the diffusing substance in equilibrium with the environment; specifically, the diffusion of the daughter product is extremely rapid compared to the production rate. This assumption makes equation (2) inappropriate in situations where a mineral may experience partial loss of some daughter product due to reheating. Dodson (1986) modified his solution to predict the spatial distribution of closure temperatures (T_c) for a sample which has undergone slow cooling (equation 4). Once again, this solution is inappropriate for predicting gradients developed when there is partial loss due to reheating and the equation is exactly true only when T^{-1} increases linearly with time.

2.4 Forward Modeling with Finite Difference Methods

In order to calculate argon profiles in biotite for a variety of cooling histories, it is either necessary to find mathematical solutions for a variety of $d\tau = f(t)\,dt$, or one can easily implement a finite difference numerical approximation of the diffusion equation. The latter approach has the advantage of flexibility, in that only one finite difference approximation can be used for a variety of thermal histories.

If we assume that diffusion is radially symmetric and that diffusion parallel to the c-axis negligible then the terms involving $\partial\theta$ and ∂z go to zero, leaving,

$$\frac{\partial C}{\partial t} = \frac{1}{r}\left\{\frac{\partial}{\partial r}\left(rD\frac{\partial C}{\partial r}\right)\right\}. \tag{16}$$

If we introduce the following non-dimensional parameters,

$$R = r/a \text{ and } \tau = Dt/a^2, \tag{17}$$

where r is the distance from the center from the grain, and a is the radius of the grain, equation (10) becomes,

$$\frac{\partial C}{\partial \tau} = \frac{1}{R}\frac{\partial}{\partial R}\left(R\frac{\partial C}{\partial R}\right) = \frac{\partial^2 C}{\partial R^2} + \frac{1}{R}\frac{\partial C}{\partial R}. \tag{18}$$

The finite-difference approximation for equation (18) is,

$$\frac{\partial C}{\partial \tau} = \frac{1}{R}\frac{\partial}{\partial R}\left(R\frac{\partial C}{\partial R}\right) = \frac{1}{2i(\delta R)^2}\left\{(2i+1)C_{i+1,j} - 4iC_{i,j} + (2i-1)C_{i-1,j}\right\}, \tag{19}$$

where $C_{i,j}$ is the concentration of the diffusing component of interest at point $(i\delta R, j\delta\tau)$, when the radius a has been divided into equal intervals of length δR, and the time-scale has been divided into regular intervals of $\delta\tau$.

For this study, equation (19) was modified to include a radiogenic production term A_j, to form,

$$C_{i,j} = \left[\left(\frac{1}{2i(\delta R)^2}\left\{(2i+1)C_{i+1,j} - 4iC_{i,j} + (2i-1)C_{i-1,j}\right\}\right)\delta\tau\right] + C_{i,j-1} + A_j. \qquad (20)$$

A_j is the amount of daughter product produced during the j-th time step, normalized by the initial amount of the parent isotope, N_0. A_j was calculated using,

$$A_j = \left(\frac{D}{N_o}\right)_j = \left(1 - \exp\left(-\lambda t_{j+1}\right)\right) - \left(1 - \exp\left(-\lambda t_j\right)\right). \qquad (21)$$

where λ, for potassium, is 5.543 x 10^{-10} a^{-1}. D, the diffusivity coefficient, was calculated for each time step assuming D followed an Arrhenius relationship (equation 1), with D_0 = .077 cm^2-sec^{-1}, E=47.0 kcal-mol^{-1} , as reported in Harrison et al, 1985. The temperature is calculated as some function of time. For all models presented in this study the edge of the grain was taken to be a free surface with zero concentration of argon. This could easily be modified by setting the concentration at $a+\delta R$ equal to some amount other than zero during each time step.

The finite difference modeling approach permits consideration of specific variables in ways not possible with analytical solutions. The initial concentration matrix, $C_{initial}$, can be set equal to any desired concentration gradient. This allows gradients to be predicted for minerals initially not in equilibrium with their environment. This method also allows one to use a variety of T=f(t) paths, allowing modeling of the effect of heating as well as cooling upon argon gradients. This is useful in predicting morphology of

argon gradients developed in minerals which experience reheating due to a short lived thermal pulse.

The finite difference numerical approximation for the diffusion of argon in biotite (equation 20) was used for a variety of T-t paths shown in Figures 1 and 2 (parameters in Table 1).

For all models presented in this study, the $C_{initial}$ was set equal to zero in order to approximate the assumption in Dodson's (1986) mathematical treatment that the grain is initially in equilibrium with the environment with respect to argon. The initial temperature, for all models, was chosen to be 800 K so that the diffusion of argon is initially very rapid relative to the production rate for a grain with a diffusion radius of 1 cm.

2.5 Results and Discussion

To compare the numerical method to Dodson's (1986) treatment, the parameters for Model A were chosen to agree with his assumptions of initial equilibrium and linear cooling with T^{-1}. The modeled concentration gradient was converted to an age gradient using,

$$t = -\frac{1}{\lambda}\ln\left(1-\frac{D}{N_o}\right). \qquad (22)$$

A closure temperature profile was then calculated by converting age to absolute temperature based on the known cooling history used in Model A. Figure 3 compares the modeled closure temperature profile for Model A, with the closure profile predicted by Dodson's equation, using the same parameters. The modeled closure temperature profile is shown with *'s. Dodson's predicted

closure profile is shown with a solid line. The agreement between closure temperatures for these two methods are within 1% of the absolute temperature.

It useful to compare the forward modeled argon gradients for T-t Models A-E. Due to the nature of the cooling trajectories, the traverse through the transitional temperature range from 730K to 550K, occurred at significantly different times. If we assume the argon accumulates more or less uniformly throughout the grain after "closure", it seems reasonable to subtract the amount of "additional" radiogenic argon trapped by the system after "closure", in order to compare the morphology of the argon gradients at the time of closure. These gradients were then normalized to facilitate comparison (Figure 4). The qualitative effect of cooling rate upon argon gradient morphology becomes apparent. Model D which experienced the most rapid descent through the transitional temperature range, has a plateau of relatively constant concentration toward the center of the grain, with a definite shoulder at the transition to lower concentrations towards the rim. This shoulder is successively less pronounced with each model traversing the transitional temperature range during a longer time span. Model E experiences the slowest traverse, and its predicted argon gradient is smooth and round. The argon gradient morphology approaches a straight line with a slope of -1, as the cooling rate approaches zero. It may be possible to use this systematic variation to estimate cooling rates for actual samples that exhibit broadly concentric age gradients. Argon gradients observed in micas by spot fusion analysis, could be normalized in the manner above, and then compared to a plot of modeled gradients to provide a rough estimate of the cooling rate. This method requires the assumption that the grain is in equilibrium with it's environment prior to onset of closure behavior. What is especially nice about

this approach is that it provides a second way of estimating cooling rate, entirely independent of Dodson's equation.

To gain insight into the ability of Dodson's method to predict closure temperatures for micas in thermal environments in which T^{-1} is not linear with time, equations (3) and (4) were applied to gradients produced by Models A through E in order to predict a closure temperature profile as one would with experimental data. In figures 5 through 8, the closure profile predicted by Dodson's method is shown with the *'s, the actual closure profile is shown with the thin solid line. From these plots it is clear that Dodson's equation does a good job estimating closure temperatures for these models, even though they arose through T-t histories that are not linear in T^{-1}.

Another way of looking at the robustness of Dodson's method is to compare the integrated cooling rate to the actual cooling path. The integrated cooling rate is calculated by taking the ages at two points on a "grain", and then calculating their respective closure temperatures using equation (20). The integrated cooling rate is the slope of the line between these two temperature-time points. Figures 9 through 12 shows the results for models B,C,D,and E. The integrated cooling rate is plotted with the thick line, along with the T-t path used to calculate each model. From these figures, it is clear that the integrated cooling rates, found by using Dodson's method, can provide a linear estimation over the transitional temperature range for cooling paths which are not linear with T^{-1}.

The diffusion radius of a mineral has a profound effect on its transitional temperature range. Smaller grains will have cooler closure temperature ranges than larger grains. Therefore, it is possible to estimate different portions of a cooling curve by calculating the integrated cooling

rates for grains of different sizes. Model F has a diffusion radius a of 1 cm, Model G has a equal to 0.1 cm. The closure temperatures for Model F are therefore higher than those for Model G (figure 13). When one calculates the integrated cooling rates from the predicted age gradients for F and G, different portions of the T-t path used to calculate F and G, is approximated (figure 14). Therefore, it is possible to approximate cooling histories that are not linear with T^{-1}, simply by combining the integrated cooling rates for a variety of samples with different closure temperature ranges.

Chapter 3

Thermal History of the Sandia Pluton

3.1 Introduction

In this chapter, I present the results from a $^{40}Ar/^{39}Ar$ thermochronologic study of the Sandia Pluton in north-central New Mexico. The Sandia pluton is a 1.45 Ga megacrystic monzogranite (Brookins and Majumdar, 1989), that belongs to a widespread 1.5-.13 Ga suite of anorogenic magmatic intrusions emplaced during the Middle Proterozoic (Anderson, 1989). This study examines the $^{40}Ar/^{39}Ar$ systematics of mica crystals in order to discern the thermal history of a mid-crustal ca. 1.4 Ga pluton in the southwest Proterozoic orogenic belt.

Using laser $^{40}Ar/^{39}Ar$ microprobe techniques, Hodges et al. (1994) studied $^{40}Ar/^{39}Ar$ systematics of muscovite and biotite from the Crazy Basin monzogranite of central Arizona, a ~1.7 Ga pluton emplaced at shallow crustal levels. Previous geochronologic data from the Crazy Basin monzogranite indicated that, subsequent to cooling to ambient temperatures, the monzogranite experienced either very slow cooling (<1K/Ma) for at least 300 Ma, or alternatively was subjected to a reheating event at 1400 - 1450 (Karlstrom and Williams, 1994). The work of Hodges et al. revealed age gradients ranging from 1650-1270 Ma in muscovite, and 1420-1150 Ma in biotite.

Such gradients are thought to be developed through thermally activated diffusion and can be a result either of slow cooling, or episodic loss due to reheating. The episodic loss hypothesis is rejected in the interpretation of the

Crazy Basin data for lack of evidence of an appropriately aged heat source. If the age gradients in the Crazy Basin micas are due to slow cooling, as suggested by Hodges et al. (1994), one might expect such a stable and long-lived thermal structure to be regionally pervasive.

Laser $^{40}Ar/^{39}Ar$ microprobe mapping of micas from the Sandia pluton supports this hypothesis. Muscovite and biotite crystals from the monzogranite exhibit argon gradients suggestive of protracted slow cooling (<<1K/Ma) after an initial thermal pulse related to intrusion and crystallization of the pluton. These gradients are incompatible with formation due to episodic loss and implicative of slow cooling and elevated geotherms through 800 Ma.

The evidence for slow cooling in the Sandia pluton and the Crazy Basin monzogranite strongly suggests that the mid-crustal thermal structure of southwestern United States Proterozoic orogen was remarkably stable over much of Middle Proterozoic time, with only transient thermal spikes related to intrusive activity such as that responsible for the Sandia Pluton.

3.2 Regional Geology

The Hudsonian craton, assembled at 1.80-1.85 Ga during the Trans-Hudson and Penokean orogenies, formed the east-northeast-trending foreland against which 1.8-1.6 Ga continental growth occurred (Van Schmus et al., 1993). This growth created a 1800 km wide, 4800 km long orogenic belt stretching from California to Labrador. In the southwestern United States, this growth has been proposed to have occurred by assembly of distinct tectonostratigraphic terranes during several pulses of convergent tectonism at 1.74, 1.70 and 1.65-1.60 Ga (Bowring & Karlstrom, 1990). Bowring and Karlstrom propose continental growth in this region to occur by assembly of

relatively thin lithospheric fragments into isostatically stable, "normal" thickness blocks of continental lithosphere.

In Arizona, these blocks have been divided into the Yavapai province and the Mazatzal province. The Yavapai province, assembled during the Yavapai orogeny at ca. 1.7 Ga, consists of five distinct tectonic blocks bounded by north- to northeast-trending shear zones (Bowring & Karlstrom, 1990). The Crazy Basin monzogranite, mentioned previously, intruded a package of 1740-1720 Ma volcanic and sedimentary rocks in the Big Bug tectonic block, of the Yavapai province (Karlstrom & Bowring, 1993).

The northeast-trending transition zone from the Yavapai to the Mazatzal province is defined by two important features in Arizona. First, there is a transition from pre -1.7 Ga basement rocks in the Yavapai province to no known outcrops of such basement rocks in the Mazatzal province. Second, the pervasive 1.70 deformation seen throughout the Yavapai province is virtually absent from the Mazatzal province, where the oldest recorded deformation is ca. 1.66 Ga. (Karlstrom & Bowring, 1993). These features are not exceptionally distinct nor diagnostic in New Mexico (Van Schmus et al., 1993). In New Mexico, the transition region between the northern limit of 1.65 Ga deformation and the southern limit of rocks older than 1.7 Ga is up to 350 km wide. The Sandia pluton lies within this transition zone. Tectonic blocks within the Mazatzal province are bounded by steeply dipping, northeast-trending shear zones, similar to those found in the Yavapai province.

Metamorphic Proterozoic rocks of northern and central New Mexico contain coexisting kyanite, andalusite, and sillimanite. This triple-point assemblage occurs in 14 separate mountain ranges over an area of 75,000 km^2 and is indicative of peak metamorphic conditions of roughly 775 K and 4kb

(Grambling et al, 1989). The absolute timing of the metamorphic event responsible for these triple-point assemblages is not constrained well. The triple-point assemblages are often found within 500 m of the overlying Proterozoic-Paleozoic unconformity. Grambling et al, (1989) suggest that this indicates little tilting of these rocks between the time of peak metamorphism and 350 Ma, the age of the oldest Paleozoic rocks at the unconformity.

The Sandia pluton is continuously exposed in the core of the Sandia Mountains of central New Mexico, directly east of Albuquerque (see Figure A). It is composed of a series of northwest-dipping sheets 5-7 km in thickness (Kirby & Karlstrom, 1993). The pluton is bounded on the southeast by a 1-2 km wide, northwest dipping, ductile shear zone, which was developed during syn-magmatic deformation (Kirby & Karlstrom, 1993). North of the shear zone, the deformed granite passes into undeformed main phase Sandia granite without a sharp structural discontinuity. To the south lies a poorly understood felsic gneiss unit, the Cibola gneiss. The Cibola gneiss and the ductile shear zone have traditionally been mapped as one unit, but the Cibola gneiss yields older apparent Rb-Sr ages than the Sandia granite (Brookins and Majumdar, 1989). Further to the south, the Cibola gneiss is separated from the Tijeras Greenstone, a 1.765-1.72 Ga basalt dominated volcano-sedimentary sequence, by the sub-vertical Tijeras fault. The absence of a contact aureole in the Tijeras greenstone has been cited as evidence that the greenstone was not in its present location relative to the Sandia granite at the time of pluton emplacement.

The northern boundary of the pluton is an intrusive contact against a metamorphosed sequence of clastic sediments, with mafic tuffs, flows, and sills (Berkley & Callendar, 1979). This sequence, the Juan Tabo Series, has an

apparent Rb-Sr age of 1.61 Ga (Brookins & Majumdar, 1982a). The thermal pulse associated with emplacement of the pluton was sufficient to develop a contact aureole in the Juan Tabo Series with zones of chlorite phyllite, andalusite schist, and sillimanite schist (Berkley and Callendar, 1979). Thermobarometric techniques indicate conditions for this contact metamorphism of 775 - 925 K, and 200-300 MPa (Berkley & Callendar, 1979), indicating that the Sandia pluton was emplaced at shallow crustal levels (<10 km).

The Sandia pluton ranges from a quartz monzogranite to granodiorite in composition. The main phase of the pluton contains megacrysts of microcline in a matrix of quartz, oligoclase, and biotite with accessory sphene, magnetite, apatite, hornblende, muscovite, pyrite and tourmaline (Brookins and Majumdar, 1989).

3.3 Statement of Purpose

This study was undertaken to illuminate the thermal history of a ca. 1.4 Ga, southwestern, Proterozoic pluton. In an attempt to find evidence for either protracted slow cooling or periodic reheating, a laser $^{40}Ar/^{39}Ar$ microprobe was used to search for argon gradients in mica crystals (cf. Hodges et al., 1994).

3.4 Experimental Techniques

In order to maximize the information available in each sample with regard to apparent age gradients, I was careful to select crystals with at least some intact crystal faces. Some crystals were picked by hand from a coarsely crushed rock; others were pulled from fresh rock faces with tweezers. The samples were washed with distilled water, acetone, and ethanol to remove any

oil or dust prior to irradiation. The samples were then packaged in an Al container, and then shielded with Cd foil.

The package was then irradiated at the McMaster University reactor. The irradiation parameter ranged from 0.014 to 0.013 $\pm$ 0.001(2σ). Flux monitor MMhb-1(520.4 Ma; Samson, 1987) was included in the package with the samples. Gas was extracted using a Coherent Innova 210 Ar-ion laser focused to it's minimum diameter. The extracted gas was purified using Al-Zr and Fe-Zr-V getters for five minutes. Isotopic analysis was then conducted with a MAP 215-50 mass spectrometer using an electron multiplier.

The laser was used at 30 to 45 amps, with a duration of contact with the sample ranging from 0.5 to 0.1 sec. The power and duration necessary to create a fusion pit was adjusted with the varying ability of the laser to couple with a sample. Fusion pits in biotite were typically 75 - 125 μm in diameter. The fusion pits for muscovite were typically 45 to 90 μm in diameter with a "dehydration zone" of up to 300μm in diameter. The "dehydration zone" consists of a discolored halo where the mineral seems to have delaminated. Each individual grain was analyzed multiple times, with melt pits being formed on the {001} cleavage plane. System blanks were measured at regular intervals and were typically two orders of magnitude smaller than the sample signal.

Apparent ages were calculated using the measurements corrected for system blanks, neutron induced interferences, and mass fractionation. The initial $^{40}Ar/^{36}Ar$ was assumed to be 295.5; decay constants used were those recommended by Steiger and Jäger (Steiger, 1977). Throughout this chapter, uncertainties are reported at the 2σ confidence level. Age uncertainties are calculated by propagating errors associated with measurement, corrections and J-value).

Integrated cooling rates and closure temperatures were calculated using the method of Dodson (1986). Diffusion parameters for biotite were taken as E=47.0±2.0 kcal mol^{-1}, and D_O = 0.077 +.21/-.06 cm^2sec^{-1}; the diffusion geometry was assumed to by cylindrical (Giletti, 1978; Harrison et al., 1985). Diffusion parameters for muscovite were calculated by a weighted linear regression of Robbins' (1973) experimental data, assuming a cylindrical diffusion geometry. The activation energy was found to be 42.01 ± 2.82 kcal mol^{-1}, with D_O = 4.023 x 10^{-4} + .0019/-8.5104 e-5 cm^2sec^{-1}. Uncertainties in integrated cooling rates and closure temperatures were obtained by Monte Carlo methods.

Samples were collected from throughout the Sandia pluton. Sample localities are shown on Figure A. $^{40}Ar/^{39}Ar$ mapping results are discussed according to location within the pluton from north to south. Fusion pits are numbered according to the sequence of analysis. Numbers are not sequential because some fusion points had either to much gas or too little gas to be reliably analyzed by the mass spectrometer. Maps of ages and associated fusion pit numbers are presented for each sample. Apparent ages and errors are given along with the apparent age calculated assuming no error in the J-value. This value was used in calculating the integrated cooling rates and closure temperatures for pairs of fusion points, because it is assumed that the J-value is identical for different points on the same grain. The sources of uncertainty for closure temperatures and integrated cooling rates are the uncertainty in the diffusion parameters and the uncertainty in the position and diffusion radius. Points near the rim have higher errors in the closure temperatures because the geometric term in Dodson's equation changes rapidly near the rim, and therefore the uncertainty in position has a greater effect near the rim. When possible the pairs of points chosen to calculate an

integrated cooling rate would be along a smooth age gradient, i.e. without obvious "troughs" of anomalously young ages.

3.5 Individual Results

SM55mu

SM55 is a muscovite crystal from the main phase Sandia granite from the northern contact with the Juan Tabo metamorphic sequence. The main phase granite becomes enriched with muscovite near this intrusive contact. This particular sample is from an outcrop 5 m from the intrusive contact.

SM55mu is 2.95 mm long and 2.25 mm wide. Apparent $^{40}Ar/^{39}Ar$ ages, obtained by laser mapping, range from 1377 $\pm$ 34 to 1296 $\pm$ 34 Ma The spatial distribution of these ages are shown in Figure B. From this Figure, it is clear that the age gradients do not form perfectly concentric gradients around the center of the grain. It is possible that this grain is actually an aggregate of grains, with the lower left lobe, consisting of points 11-15, acting as a separate diffusion environment. Note, that the oldest age in the center of this region (1377 Ma, point 13) is the same age as in the center of the upper right lobe(1377 Ma, point 16). When this crystal is treated as two crystals, the cooling rates obtained by applying Dodson's (1986) treatment yields average integrated cooling rates of -1.6 K/Ma for the upper right zone, and -2.1 K/Ma for the lower left zone.

SM32mu

SM32mu is a muscovite crystal from a pegmatitic dike within the main phase of the Sandia granite, (see Figure A for sample locality). SM32mu is ~2.9 mm long and ~2.1 mm wide. This muscovite yielded apparent $^{40}Ar/^{39}Ar$ ages

ranging from 1394 ±34 to 1331±34 Ma . The spatial distribution of these ages is shown in Figure C. The oldest age, point 13, is slightly off center. Since this age was not found at a pristine crystal edge, this may be due to breakage of the crystal during preparation. The ages do form loosely concentric gradients about point 13. The average integrated cooling rate is -0.9 K/Ma through the closure interval.

SM33bt

SM33bt is a biotite crystal from the main phase of the Sandia granite. This sample is from the same outcrop as SM32mu. SM33bt is 1.7 mm in length and 1.26 mm wide. Apparent $^{40}Ar/^{39}Ar$ ages range from 1257±50 to 790±23 Ma (Figure D). The oldest ages are off center relative to the edges of the grain, however, the edge they are closest to does not appear to be a primary crystal face, therefore, this sample could have been broken during preparation. The ages form broadly concentric gradients away from the zone of older ages. These ages yield an average integrated cooling rate of -0.075 K/Ma.

SM63bt

SM63bt is a biotite sample from a sample of main phase Sandia granite from Embudito canyon (Figure A). SM63bt is 2.4 mm long and 1.8 mm wide. Apparent $^{40}Ar/^{39}Ar$ ages range from 1325 ± 28 to 1110 ± 24 Ma (Figure E). This crystal has a "ridge" of older ages in with ages decreasing as one moves away from this central ridge. Perhaps this is an artifact of breakage during preparation. These ages yield a average integrated cooling rate of -0.19 K/Ma.

SM62bt

SM62bt is a biotite crystal from a sample of main phase Sandia granite from Embudo canyon (see Figure A). SM62bt is 2.6 mm long and 2.1 mm wide. The laser mapping revealed apparent $^{40}Ar/^{39}Ar$ ages ranging from 1387 $\pm$ 29 Ma to 1230 $\pm$ 26 Ma (Figure F). The average integrated cooling rate is -0.49 K/Ma.

3.6 Discussion and Suggestions for Further Study

The age gradients found in these samples by $^{40}Ar/^{39}Ar$ microprobe mapping, are not generally smooth, perfectly concentric in nature, or centered relative to the edges of the crystal. If we assume these gradients are generated by thermally activated diffusion, they have irregularities that require some explanation. Detailed age mapping by Hames and Hodges (1993) and Hodges et al. (1994) revealed troughs of younger ages in other slowly cooled samples. These were interpreted to be fast diffusion paths with in the crystal lattice. In one case, these fast diffusion paths formed a 120^{o} angle, highly suggestive that, at least in this case, the fast diffusion paths were subgrain boundaries related to cleavages. In this study, high-precision mapping was sacrificed in the interest of analyzing as many different samples as possible. It seems possible that some of the irregularities in the age gradients may be due to fast diffusion paths, but I feel that drawing detailed topographic maps of age gradients would require over-interpretation of the available data for these samples, and therefore inappropriate.

The variety in the youngest apparent ages is strongly suggestive that the age gradients are not due to episodic loss of argon by reheating. When a mineral experiences episodic loss due to reheating, the material closest to the

free surface (edge of the grain) loses virtually all of the diffusing substance present. Thus, a mineral which experienced this sort of loss of radiogenic argon, the youngest apparent age near the rim should provide a maximum estimate of the timing of the reheating event. For argon gradients in the Sandia samples to be formed by reheating, there would need to be thermal pulses at ~1331 Ma, ~1296 Ma, ~1230 Ma, ~1110 Ma, and ~790 Ma, if we assume these samples are relatively intact. Due to absence of evidence for five appropriately aged heat sources, the episodic loss hypothesis is extremely unlikely.

The episodic loss hypothesis is also unlikely due to the disparity of youngest apparent age for SM32mu (1331 Ma) and SM33bt (790 Ma). In order for these gradients to be developed by reheating, it would require two thermal pulses. The second pulse would need to be sufficient to reset SM33bt to 790 Ma, yet cool enough and brief enough, to have no effect on the argon in SM32mu, collected a mere 3m from SM33bt.

When the closure temperatures and cooling rates are plotted versus apparent ages for all calculations for all samples, a remarkably coherent curve is obtained (Figure most excellent). As reported in section 2.5, argon gradients developed by cooling histories that are not linear in T^{-1}, can still provide an integrated cooling rate that is tangential to the cooling curve at the transitional temperature range. Different minerals record different portions of the cooling curve due to the variability in closure temperature. The closure temperature range is highly dependent on the size of the grain and diffusion parameters. A variety of grain sizes and minerals can collectively define a cooling curve by approximating different portions of the curve. Therefore SM32mu, a large muscovite records a higher temperature portion of the

cooling path, than SM33bt, a smaller biotite grain. The coherence of the cooling curve in Figure most excellent suggests that the five samples from the Sandia pluton are collectively approximating the cooling history of the Sandia pluton. If we assume that Figure most excellent represents a portion of the cooling history of the Sandia pluton, the Sandia pluton experienced a thermal pulse most likely associated with its intrusion and crystallization. After this transient thermal spike, the plutonic samples record an episode of stable, protracted slow cooling.

It is possible that age gradients could be formed due to chemical zoning within a crystal. If there is an initial potassium gradient, there will a production gradient for radiogenic argon. If the sample cools very rapidly, a radiogenic argon gradient will be preserved due to the initial potassium gradient, yet there will be no apparent age gradient, because the radiogenic argon will be supported by a proportional potassium gradient. If there is an initial gradient with a higher concentration of potassium in the center of the grain, there will be higher radiogenic production in towards the center of the grain. If we assume for the purposes of this thought experiment that no argon is lost from the system, the argon gradient will drive diffusion of argon until there is a uniform distribution of argon. An apparent age gradient will exist with older ages towards the rim, where argon produced in the high-production (potassium-rich) areas has flowed into lower-production (potassium-poor) areas. There will be younger apparent ages towards the center of the grain where argon produced in this region has diffused towards lower concentration region. In a situation where there is an initial potassium gradient that is elevated at the edges, the radiogenically produced argon will flow towards the low concentration center of the grain, this will produce older

apparent ages in the center of the grain, progressively younger edges towards the rim.

Research by Harrison et al, (1985) indicates some compositional control on the diffusivity of argon in biotite. The diffusivity of argon increases with increasing Fe/Fe+Mg content. I would predict that biotite grain with lower Fe/Fe+Mg in the center of a grain and Fe/Fe+Mg towards the rim, will tend to have older ages in the Fe-poor zones, and younger ages in the Fe-rich edges, than a grain with an intermediate, homogeneous composition, all other things being equal. In the reverse situation, a grain with Fe-rich core I would expect the argon gradient to have a flatter morphology. The ages near the rims would most likely be older than in an intermediate, homogeneous grain. The low diffusivity of the rims would limit the escape of argon from the center of the grain, creating an argon gradient with little topography. Thus, when applying Dodson's method for calculating integrated cooling rates, a biotite with a Fe-rich center may give anomalously rapid cooling rates, and a biotite crystal with Fe-rich rims would tend to give anomalously slow cooling rates, . These predictions for the effect of composition could easily be checked by running a number of finite difference models for the diffusion equation, where the diffusivity would vary with position, or the amount of radiogenic argon produced during each time step would vary with position.

In order to eliminate the possibility that gradients have been effected by chemical variations within mineral grains, it will be necessary to do microprobe analysis on samples from the Sandia pluton.

Another issue that should be considered is the effect of the increasing concentration of vacancies in the potassium site. While a mineral is in equilibrium with respect to the environment, a vacancy is produced in the

potassium site every time a potassium atom decays to radiogenic argon, which in turn diffuses out of the system. The concentration ratio of radiogenic/diffusion produced potassium-vacancies to originally filled potassium-sites can be calculated by using,

$$\frac{D}{N_o} = 1 - \exp\left[-\lambda\left(t_{crystalization} - t_{apparentage}\right)\right]$$

Where D is the amount of daughter isotope produced after crystallization and prior to the time recorded by the apparent age. By definition, this quantity of daughter product must be lost to the environment to obtain an apparent age different from the crystallization age. For every daughter product lost to the environment, a vacancy is produced in a potassium site. The value D/N_O is most likely not the absolute concentration of vacancies at the time of closure. During crystallization there are probably some vacancies formed in the crystal structure as point defects. The concentration of these initial vacancies are described in simpler physical systems in terms of an equilibrium concentration of vacancies that minimizes the entropy of the system at a particular temperature. For a complex process such as the formation of biotite from a magma melt, calculation of the equilibrium concentration of vacancies in the potassium site is non-trivial. The term D/N_O gives the additional vacancies created over time beyond this initial concentration of vacancies. The situation is complicated by the fact that vacancies can diffuse through a substance and be lost at the surface of a system, when the concentration within the grain is higher than the equilibrium concentration for a given temperature. I know of no estimates for the diffusivity of potassium-site vacancies in micas, but if we assume that the diffusivity of potassium-vacancies is slower than the diffusion of argon, over time a significant number of potassium-vacancies could be produced in the crystal lattice. For

example, if we assume that sample SM33bt crystallized at 1450 Ma, by the time the center of the grain exhibits closed behavior at 1223 Ma, 10% of the potassium atoms have decayed to argon and then diffused out of the mineral. By the time the rim exhibits closed behavior, 30% of the original potassium atoms have undergone radioactive decay, and the produced argon has escaped the system. We might then expect the center of the grain to have at least 10% of the potassium sites vacant, and the rim of the crystal to have at least 30% of these site vacant. The atomistic process by which argon diffuses out of a mica crystal lattice is not well understood. Given a cylindrical diffusion geometry, this may be accomplished by a vacancy mechanism, in which an argon atom would move through the crystal lattice by jumping into an adjacent unoccupied site. Intuitively, if argon diffuses by jumping from potassium-site to potassium-site, the greater the concentration of potassium-site-vacancies, the easier it would be for argon to diffuse through the system. If there is a strong correlation between potassium-site vacancies and the diffusivity of argon in micas, the difference between 10% and 30% vacant potassium may have a significant effect on diffusivity within the grain, and therefore on closure temperatures. For SM33bt, the points at 1223 Ma and 790 Ma yield an integrated cooling rate of ~-0.06 K/Ma, with closure temperatures of 584 K and 559 K respectively. This calculation assumes that the diffusivity of argon is constant throughout the grain, varying uniformly only with the temperature of the system. Let's assume the diffusion constants used to estimate the integrated cooling rate are correct for the center of the grain, and we assume the higher vacancy concentration near the rim increases the diffusivity, the estimate of a closure temperature for the point at the rim may be too high. Therefore, the cooling rate, in this situation, may appear slower than it actually is.

Chapter 4

Conclusions

The principal conclusions of this study are:

(1) Dodson's (1986) equations can predict, with reasonable accuracy, closure temperature profiles for slowly cooled samples which experience cooling paths that are not linear with T^{-1}.

(2) Integrated cooling rates, found by using Dodson's (1986) equations, provide a linear approximation of the cooling curve at the transitional temperature range. The linear approximation is good even when the cooling history is not linear with T^{-1}.

(3) Different portions of a cooling curve can be approximated by analyzing a suite of minerals with different transitional temperature ranges. A collection of integrated cooling rates can define a portion of a cooling history.

(4) The thermal history of the Sandia pluton of New Mexico experienced a transient thermal pulse related to emplacement and crystallization, followed by protracted slow cooling. The cooling history obtained for the Sandia pluton, when considered with the results from the Crazy Basin monzogranite (Hodges et al., 1994), provide strong evidence for regional slow cooling at shallow crustal levels throughout the Middle Proterozoic

References

Anderson J. L. (1989) Proterzoic anorogenic granites of the southwestern United States. In *Geologic Evolution of Arizona* (ed. Jenney J. P. and Reynolds S. J.), pp.211-238. Arizona Geological Digest, v.17.

Berkley J. L., and Callender J. F. (1979) Precambrian metamorphism in the Placitas-Juan Tabo area, northwestern Sandia Mountains, New Mexico: New Mexico Geological Society 30th Field Conference Guidebook, p. 181-188.

Bowring S.A., Karlstrom K.E. (1990) Growth, stabilization, and reactivation of Proterozoic lithosphere in the southwestern United States: *Geology*. **18**, 1203-1206.

Brookins B. D., and Majumdar A. (1989) Geochronologic study of Precambrian rocks of the Sandia Mountains, New Mexico. In *Proterozoic geology of the southern Rocky Mountains* (eds Grambling J.A. and Tewksbury B.J.), pp. 87-110. Geological society of America Special Paper 235.

Crank J. (1975) *The Mathematics of Diffusion*, 414 pp., Clarendon, Oxford.

Dodson M. H. (1973) Closure Temperature in Cooling Geochronological and Petrological Systems: *Contributions to Mineralogy and Petrology*. **40**, 259-247.

Dodson M. H. (1986) Closure Profiles in Cooling Systems: *Materials Science Forum*. **7**, 145-154.

Hames W. E. and Hodges K.V. (1993) Laser $^{40}Ar/^{39}Ar$ Evaluation of Slow Cooling and Episodic Loss of ^{40}Ar from a Sample of Polymetamorphic Muscovite: *Science*. **261**, 1721-1723.

Harrison, T. M., Duncan I, and MacDougall I., 1985, Diffusion of ^{40}Ar in Biotite: Temperature, pressure and Compositional Effects: *Geochemica et Cosmochimica Acta*. **49**, 2461-2468.

Hodges K. V., Hames W. E., Bowring S. A. (1994) $^{40}Ar/^{39}Ar$ age gradients in micas from a high-temperature-low-pressure metamorphic terrain: Evidence for very slow cooling and implications for the interpretations of age spectra: *Geology*. **22**, 55-58.

Grambling J. A., Williams M. L., Smith R.F., and Mawer C. K. (1989) The role of crustal extension in the metamorphism of Proterozoic rocks in northern New Mexico. In *Proterozoic geology of the southern Rocky Mountains* (eds Grambling J.A. and Tewksbury B.J.), pp. 87-110. Geological society of America Special Paper 235.

Giletti B. J. (1974) Studies in Diffusion I: Argon in phlogopite mica. In *Geochemical Transport and Kinetics* (ed. Hofmann A. W. et al.), pp 107-115. Carnegie Institute of Washingtom Publication.

Karlstrom K.E. and Bowring S.A. (1993) Proterozoic orogenic history of Arizona. In *Precambrian: Conterminous U. S.* (eds. Reed J.C., Bickford M. E., Houston R. S., Link P. K., Rankin D. W., Sims D. W. and Van Schmus W. R.), pp. 188-211. DNAG, **C-2**.

Karlstrom K. E. and Williams M. L. (1994) The case for simultaneous deformation, metamorphism, and plutonism: Am example from Proterozoic rocks in central Arizona: *Journal of Stuctural Geology* (in press).

Kirby E. and Karlstrom K.E. (1993) Emplacement of the 1.42 Ga Sandia pluton, N. M.: A record of middle Proterozoic tedtonism: *Geological Society of America Abstracts with Programs*, **25**, no. 6, p. A304.

Samson S. D. and Alexander E. C. (1987) Calibration of the interlaboratory $^{40}Ar/^{39}Ar$ dating standard, MMhb-1: *Chemical Geology*. **66**, 27-34.

Shewmon P. (1989) *Diffusion in Solids*. 246 pp., The Minerals, Metals & Materials Society.

Steiger J. H. and Jäger E. (1977) Subcommission on geochronology: convention onthe use of decay constants in geo- and osmochronology: *Earth and Planetary Science Letters*. **36**, 359-362.

Van Schmus W. R., Bickford M. E. and Condie K.C. (1993) Early Proterozoic crustal evolution. In *Precambrian: Conterminous U. S.* (eds. Reed J.C., Bickford M. E., Houston R. S., Link P. K., Rankin D. W., Sims D. W. and Van Schmus W. R.), pp. 270-281. DNAG, **C-2**.

Table Captions

Table 1. Model Parameters

Table 2. SM55mu $^{40}Ar/^{39}Ar$ Apparent Ages

Table 3. SM55mu Integrated Cooling Rates and Closure Temperatures

Table 4. SM32mu $^{40}Ar/^{39}Ar$ Apparent Ages

Table 5. SM32mu Integrated Cooling Rates and Closure Temperatures

Table 6. SM33bt $^{40}Ar/^{39}Ar$ Apparent Ages

Table 7. SM33bt Integrated Cooling Rates and Closure Temperatures

Table 8. SM63bt $^{40}Ar/^{39}Ar$ Apparent Ages

Table 9. SM63bt Integrated Cooling Rates and Closure Temperatures

Table 10. SM62bt $^{40}Ar/^{39}Ar$ Apparent Ages

Table 11. SM62bt Integrated Cooling Rates and Closure Temperatures

Table 1. Model Parameters

	Model A	Model B	Model C	Model D	Model E	Model F	Model G
Initial T	800	800	800	800	800	800	800
Final T	400	400	400	400	400	500	500
Elapsed time (Ma)	400	400	400	400	400	400	400
Linearity	1/T	1/T^2	1/T^4	1/T^10	T^10	1/T^10	1/T^10
Diffusion Radius (cm)	1	1	1	1	1	1	0.1

Table 2. SM55mu 40Ar/39Ar Apparent Ages

Spot Number	39Ar/40Ar (x10^-2)	36Ar/40Ar (x10^-5)	40Ar* (%)	Age (Ma)	Error 2σ	No J-value error 2σ
1	1.169	1.286	99.62	1361	35	0.1
2	1.188	0.673	99.80	1347	34	0.2
3	1.166	0.052	99.98	1367	35	0.5
4	1.178	3.005	99.11	1349	34	0.2
5	1.190	1.488	99.56	1343	34	0.8
6	1.175	0.871	99.74	1358	35	1.4
7	1.248	1.507	99.55	1299	34	0.5
8	1.243	0.925	99.73	1305	34	1.3
9	1.189	2.600	99.23	1341	34	0.9
10	1.190	0.335	99.90	1347	34	0.3
11	1.211	12.256	96.38	1297	34	0.0
12	1.164	1.109	99.67	1366	35	0.3
13	1.153	0.251	99.93	1377	35	0.2
14	1.159	1.223	99.64	1369	35	0.8
15	1.195	0.291	99.91	1343	35	3.7
16	1.152	0.495	99.85	1377	35	0.5
17	1.187	1.801	99.47	1346	34	1.0
18	1.202	3.798	98.88	1328	34	1.0
19	1.188	1.943	99.43	1344	34	1.9
20	1.167	1.823	99.46	1361	35	1.2

Table 3. SM55mu Integrated Cooling Rates and Closure Temperatures

center point	rim point	Tc center (K)	Tc center error 2s	Tc rim (K)	Tc rim error 2s	cooling rate (K/Ma)
16	18	638	92	582	220	-1.12
16	15	677	97	629	89	-1.4
16	9	660	98	525	224	-3.74
13	15	642	97	514	306	-3.78
13	11	607	89	572	240	-0.435
					average cooling rate	-2.095

Table 4. SM32mu 40Ar/39Ar Apparent Ages

Spot Number	39Ar/40Ar (x10^-2)	36Ar/40Ar (x10^-5)	40Ar* (%)	Age (Ma)	Error 2σ	No J-value error 2σ
2	1.170	1.345	99.60	1360	35	0.2
3	1.197	3.919	98.84	1331	34	1.2
4	1.185	5.285	98.44	1337	34	1.1
5	1.168	1.593	99.53	1361	35	0.2
7	1.143	1.535	99.55	1382	35	0.4
8	1.182	2.108	99.38	1348	34	0.3
9	1.174	1.004	99.70	1362	35	0.5
10	1.166	5.580	98.35	1365	35	0.7
11	1.168	2.037	99.40	1367	35	0.8
12	1.191	1.200	99.65	1370	34	1.3
13	1.132	0.553	99.84	1372	35	3.5
14	1.147	1.162	99.66	1375	35	2.8
15	1.192	6.769	98.00	1378	34	0.9
16	1.156	1.241	99.63	1380	35	0.4
17	1.182	1.833	99.46	1383	34	1.1

Table 5. SM32mu Integrated Cooling Rates and Closure Temperatures

center point	rim point	Tc center (K)	Tc center error 2σ	Tc rim (K)	Tc rim error 2σ	cooling rate (K/Ma)
13	12	644	92	604	117	-0.80
7	12	648	90	632	85	-0.43
7	15	622	82	617	79	-0.09
7	4	644	91	594	177	-1.09
7	3	657	87	624	79	-0.65
16	17	654	91	617	114	-1.61
2	12	665	91	649	85	-0.55
2	3	669	91	634	82	-1.21
2	10	671	95	659	91	-1.00
					average cooling rate	-0.82

Table 6. SM33bt 40Ar/39Ar Apparent Ages

Spot Number	39Ar/40Ar (x10^-2)	36Ar/40Ar (x10^-4)	40Ar* (%)	Age (Ma)	Error 2σ	No J-value error 2σ
1	1.653	1.385	95.91	1027	45	1.7
2	1.568	1.256	96.29	1072	46	0.9
3	1.768	1.451	95.71	974	43	1.3
4	1.621	1.424	95.79	1041	45	2.0
5	1.672	1.198	96.46	1023	45	1.6
6	1.583	0.863	97.45	1074	46	0.8
7	1.761	1.020	96.99	987	44	2.4
8	1.517	0.764	97.74	1112	47	1.1
9	1.582	0.824	97.57	1076	46	1.8
10	1.642	1.041	96.92	1040	45	0.8
11	1.487	1.271	96.24	1115	48	1.7
12	1.374	0.805	97.62	1195	50	7.2
13	1.344	0.553	98.37	1221	51	1.3
14	1.399	0.473	98.60	1188	50	0.5
15	1.342	0.515	98.48	1223	51	1.2
16	1.418	0.566	98.33	1174	49	2.0
17	1.411	0.551	98.37	1179	49	1.1
18	1.348	0.806	97.62	1211	50	0.3
19	1.810	1.270	96.25	960	29	9.5
20	2.001	2.052	93.94	871	25	1.9
21	1.864	1.200	96.46	940	27	6.3
22	2.267	1.913	94.35	791	23	2.7
23	1.632	0.507	98.50	1058	29	0.5
24	1.785	0.616	98.18	986	28	0.5
25	1.567	0.427	98.74	1093	30	1.2

Table 7. SM33bt Integrated Cooling Rates and Closure Temperatures

center point	rim point	Tc center (K)	Tc center error 2σ	Tc rim (K)	Tc rim error 2σ	cooling rate (K/Ma)
18	19	586	29	586	28	-0.06
18	21	596	30	569	31	-0.10
18	21	594	30	576	29	-0.07
15	22	584	29	559	36	-0.06
15	21	586	31	557	75	-0.10
15	19	579	29	565	28	-0.05
13	7	595	29	571	29	-0.10
					average cooling rate	-0.08

Table 8. SM63bt 40Ar/39Ar Apparent Ages

Spot Number	39Ar/40Ar (x10^-2)	36Ar/40Ar (x10^-4)	40Ar* (%)	Age (Ma)	Error 2σ	No J-value error 2σ
1	1.217	2.389	92.94	1287	27	0.1
2	1.489	2.430	92.82	1110	24	0.5
3	1.299	2.623	92.25	1222	26	0.8
4	1.254	1.473	95.65	1286	27	0.9
5	1.215	2.122	93.73	1297	27	0.4
11	1.256	2.622	92.25	1252	27	0.6
12	1.281	1.787	94.72	1258	27	0.8
13	1.323	1.506	95.55	1237	26	0.4
15	1.372	2.555	92.45	1176	25	0.7
16	1.454	2.921	91.37	1117	25	1.0
19	1.365	1.541	95.45	1208	26	0.7
21	1.417	1.190	96.49	1185	26	1.0
22	1.379	1.453	95.71	1202	26	1.6
23	1.497	1.705	94.96	1125	25	3.1
24	1.335	1.834	94.58	1220	26	0.7
25	1.336	1.919	94.33	1217	26	0.3
26	1.329	1.685	95.02	1228	26	1.2
27	1.361	0.432	98.72	1241	26	0.2
28	1.395	0.640	98.11	1214	26	0.4
29	1.379	0.473	98.60	1228	26	0.4
30	1.283	1.020	96.99	1278	27	0.6
31	1.284	1.012	97.01	1278	27	0.4
32	1.348	0.872	97.42	1238	26	0.3
33	1.281	0.606	98.21	1291	27	0.4
34	1.304	0.421	98.76	1280	27	0.2
35	1.326	0.788	97.67	1255	27	0.2
36	1.291	0.520	98.46	1287	27	0.3
37	1.294	0.314	99.07	1290	27	0.6
38	1.252	0.140	99.59	1325	28	0.8
39	1.395	0.802	97.63	1209	26	1.0
40	1.351	1.083	96.80	1230	26	0.4

Table 9. SM63bt Integrated Cooling Rates and Closure Temperatures

center point	rim point	Tc center (K)	Tc center error 2σ	Tc rim (K)	Tc rim error 2σ	cooling rate (K/Ma)
36	2	588	31	561	64	-0.15
5	23	585	30	568	29	-0.10
1	23	575	31	565	29	-0.06
31	24	591	31	582	30	-0.16
4	39	599	31	570	74	-0.36
34	22	593	31	579	34	-0.18
34	19	584	32	574	32	-0.15
36	40	586	31	578	29	-0.14
33	2	599	33	560	107	-0.22
					average cooling rate	-0.17

Table 10. SM62bt 40Ar/39Ar Apparent Ages

Spot Number	39Ar/40Ar (x10^-2)	36Ar/40Ar (x10^-5)	40Ar* (%)	Age (Ma)	Error 2σ	No J-value error 2σ
1	1.233	3.532	98.96	1334	28	0.6
2	1.222	6.929	97.95	1332	28	2.0
5	1.284	9.947	97.06	1278	27	1.0
6	1.191	20.024	94.08	1319	28	0.8
7	1.263	4.121	98.78	1310	27	0.4
8	1.185	2.736	99.19	1374	28	0.3
9	1.237	4.315	98.72	1329	28	0.6
13	1.264	1.634	99.52	1316	28	0.8
14	1.335	3.462	98.98	1260	27	1.0
15	1.341	2.345	99.31	1259	27	1.4
16	1.292	8.525	97.48	1276	27	1.4
17	1.255	1.781	99.47	1322	28	1.2
18	1.268	3.966	98.83	1306	27	0.6
19	1.231	7.285	97.85	1325	28	0.4
20	1.183	2.896	99.14	1375	28	0.7
21	1.194	5.079	98.50	1360	28	0.5
22	1.242	4.209	98.76	1325	28	3.1
23	1.233	5.381	98.41	1329	28	2.0
24	1.212	1.691	99.50	1356	28	0.1
25	1.233	0.578	99.83	1342	28	1.5
26	1.260	4.800	98.58	1310	28	2.5
27	1.260	5.062	98.50	1309	27	1.1
28	1.220	1.378	99.59	1350	28	1.9
29	1.225	1.509	99.55	1346	28	0.8
30	1.265	1.317	99.61	1316	28	1.2
31	1.278	1.584	99.53	1306	27	0.9
32	1.306	0.843	99.75	1288	27	1.5
35	1.304	4.308	98.73	1279	27	0.9
36	1.314	2.541	99.25	1278	27	2.0
37	1.244	1.334	99.61	1332	28	4.6
38	1.243	2.581	99.24	1329	28	0.8
39	1.173	1.430	99.58	1387	29	1.0
40	1.230	1.770	99.48	1341	28	1.2
43	1.247	1.295	99.62	1329	28	0.8
44	1.261	2.549	99.25	1315	28	0.4

Table 11. SM62bt Integrated Cooling Rates and Closure Temperatures

center point	rim point	Tc center (K)	Tc center error 2σ	Tc rim (K)	Tc rim error 2σ	cooling rate (K/Ma)
21	32	627	34	578	78	-0.68
21	31	624	29	594	31	-0.55
21	30	613	31	601	29	-0.27
21	29	623	30	616	29	-0.53
8	16	622	33	528	148	-0.97
28	32	622	34	579	81	-0.70
8	36	602	32	570	82	-0.33
8	15	604	32	570	76	-0.29
8	7	554	29	553	28	-0.01
8	15	605	33	567	92	-0.33
8	17	614	31	587	33	-0.52
					average cooling rate	-0.47

Figure Captions

Figure 1. Models A through E were calculated with cooling paths which at t=0, were at 800 K and cooled to 400 K over 400 Ma. Cooling path A, shown by the dotted line, increases linearly with T^{-1}, path B (o) increases linearly with T^{-2}, path C (*) increases linearly with T^{-4}, path D (x) increases linearly with T^{-10}, and path E (+) increases linearly with T^{10}. All of these models were calculated using a diffusion radius a equal to 1 cm, with a spatial resolution 0.01 cm.

Figure 2. Models F and G were calculated with a cooling trajectory (solid line) which was linear with T^{-10}, initially at 800K and cooling to 500K over 400 Ma. The dotted line shows the cooling path which has the same initial and final temperatures, but is linear with T^{-1}

Figure 3. Model A, modeled closure temperature profile (*), and closure profile predicted by Dodson's (1986) equation.

Figure 4. Normalized concentration gradients for Models A - E: Model A (_._._); Model B (o); Model C (*); Model D (X) and Model E (+). r is the distance from center of the grain and a is the radius of the grain.

Figure 5. Model A predicted closure temperature profile (solid line) with inverse modeled closure temperature profile (*).

Figure 6. Model B predicted closure temperature profile (solid line) with inverse modeled closure temperature profile (*).

Figure 7. Model C predicted closure temperature profile (solid line) with inverse modeled closure temperature profile (*).

Figure 8. Model E predicted closure temperature profile (solid line) with inverse modeled closure temperature profile (*).

Figure 9. Model B inverse modeled integrated cooling rate (thick line) with actual T-t path used in simulation.

Figure 10. Model C inverse modeled integrated cooling rate (thick line) with actual T-t path used in simulation.

Figure 11. Model D inverse modeled integrated cooling rate (thick line) with actual T-t path used in simulation.

Figure 12. Model E inverse modeled integrated cooling rate (thick line) with actual T-t path used in simulation.

Figure 13. Models F and G, modeled closure temperature profiles.

Figure 14. Models F and G inverse modeled integrated cooling rates (thick lines) with actual T-t path used in simulation.

Figure 15. Location of Sandia Mountains.

Figure 16. Simplified Geologic Map of Sandia Mountains, with sample localities.

Figure 17. SM55, muscovite, map of apparent age gradient with fusion spot locations.

Figure 18. SM32, muscovite, map of apparent age gradient with fusion spot locations.

Figure 19. SM33, biotite, map of apparent age gradient with fusion spot locations.

Figure 20. SM63, biotite, map of apparent age gradient with fusion spot locations.

Figure 21. SM62, biotite, map of apparent age gradient with fusion spot locations.

Figure 22. Collective integrated cooling rates for Sandia samples. SM55 (....), SM32 (----). SM33 (solid line), SM63 (thick solid line), SM63 (_._.).

Figure 1.

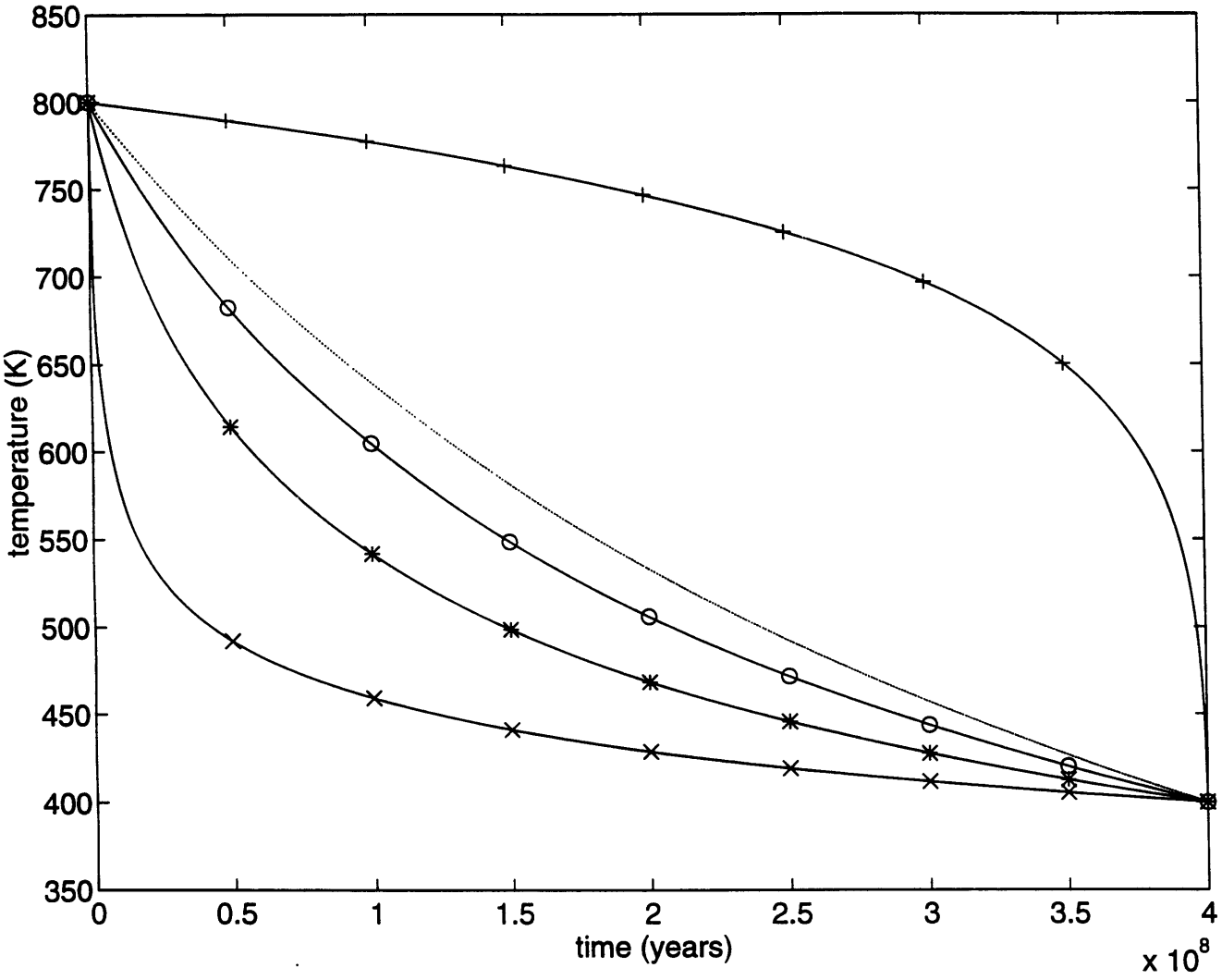
850
800
750
700
650
600
550
500
450
400
350
temperature (K)
0
0.5
1
1.5
2
2.5
3
3.5
4
time (years)
x 10^8

Figure 2.

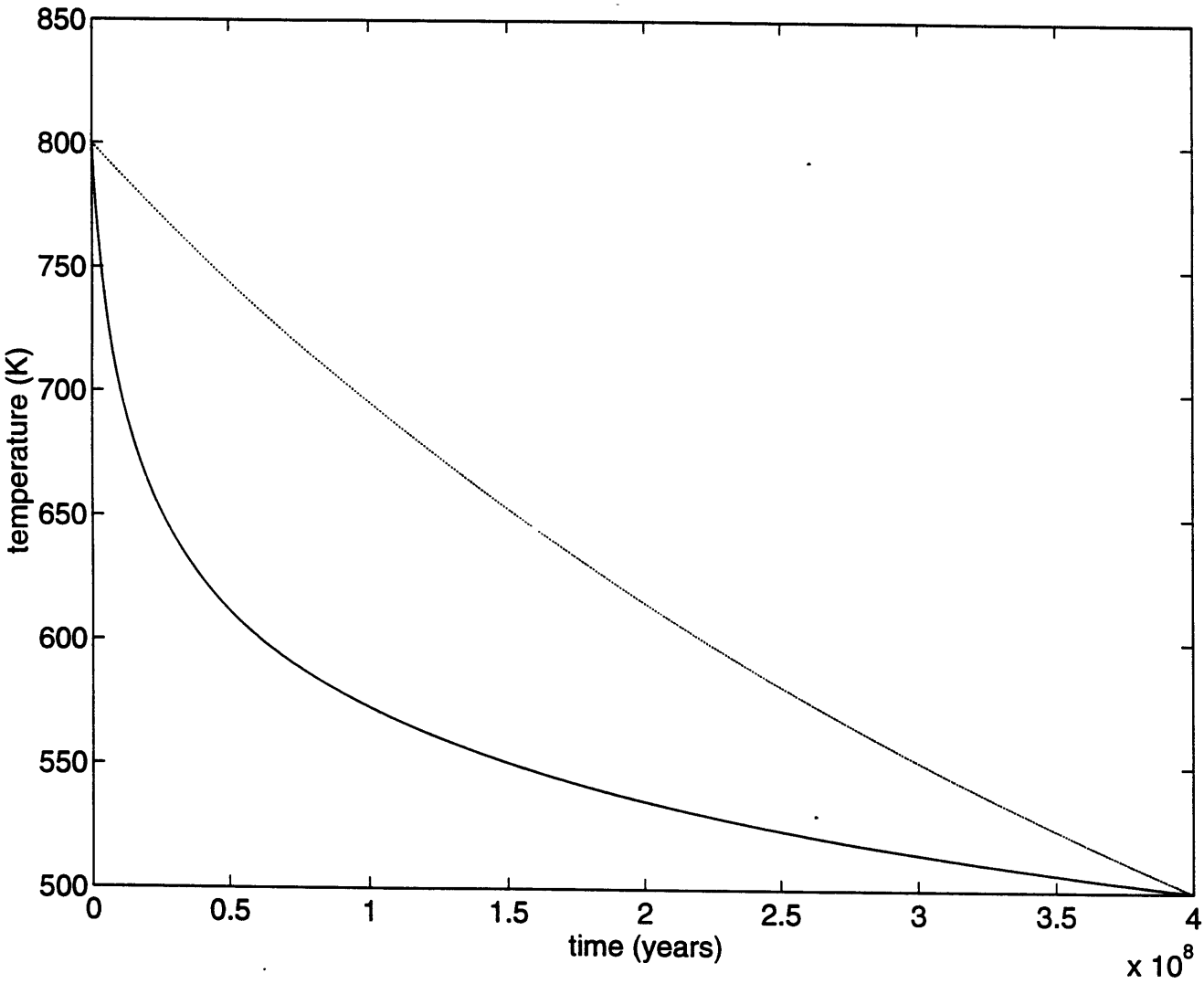
850
800
750
700
650
600
550
500
temperature (K)
0
0.5
1
1.5
2
2.5
3
3.5
4
time (years)
x 10^8

Figure 3.

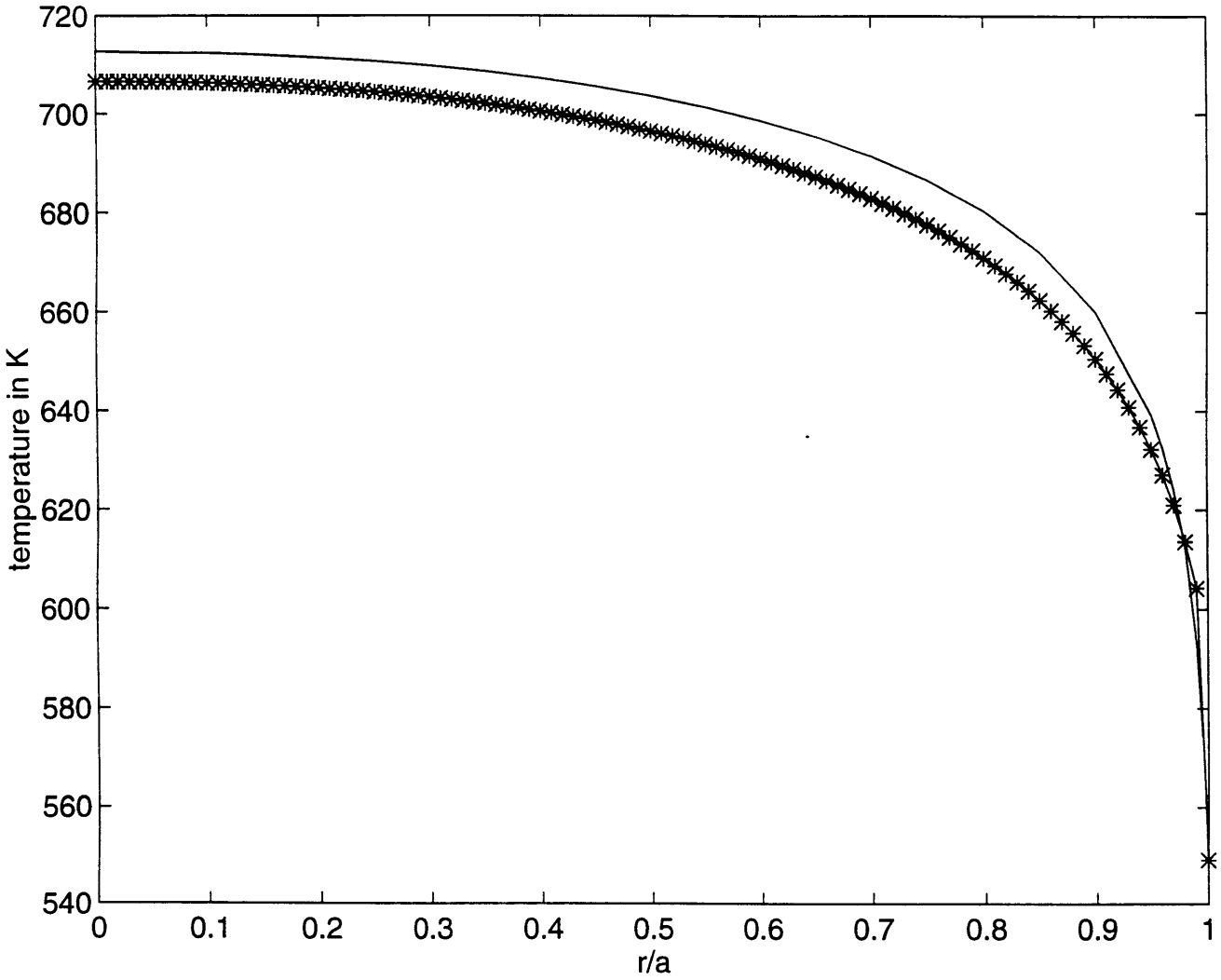
720
700
680
660
640
620
600
580
560
540
temperature in K
0
0.1
0.2
0.3
0.4
0.5
0.6
0.7
0.8
0.9
1
r/a

Figure 4.

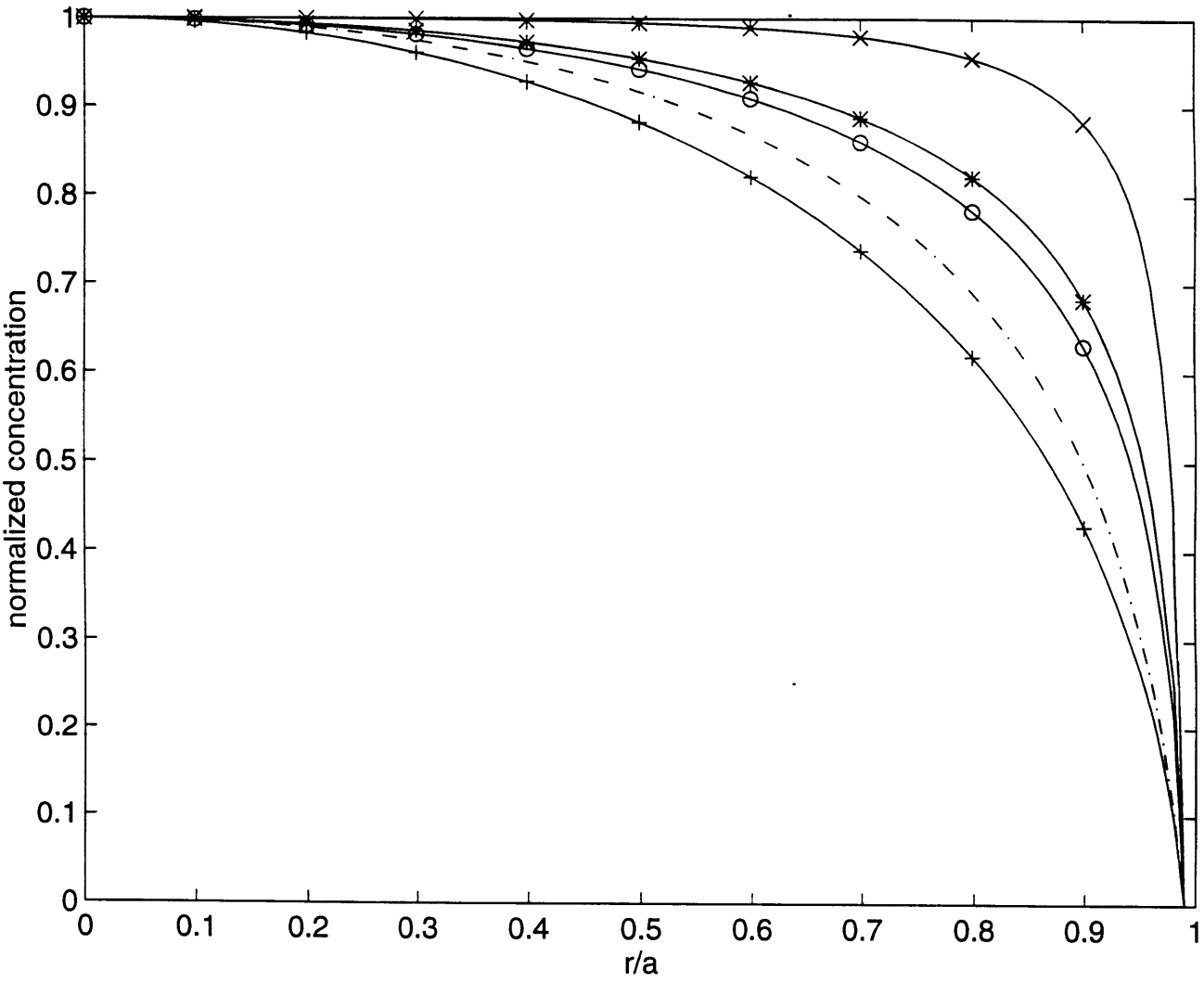

Figure 5.

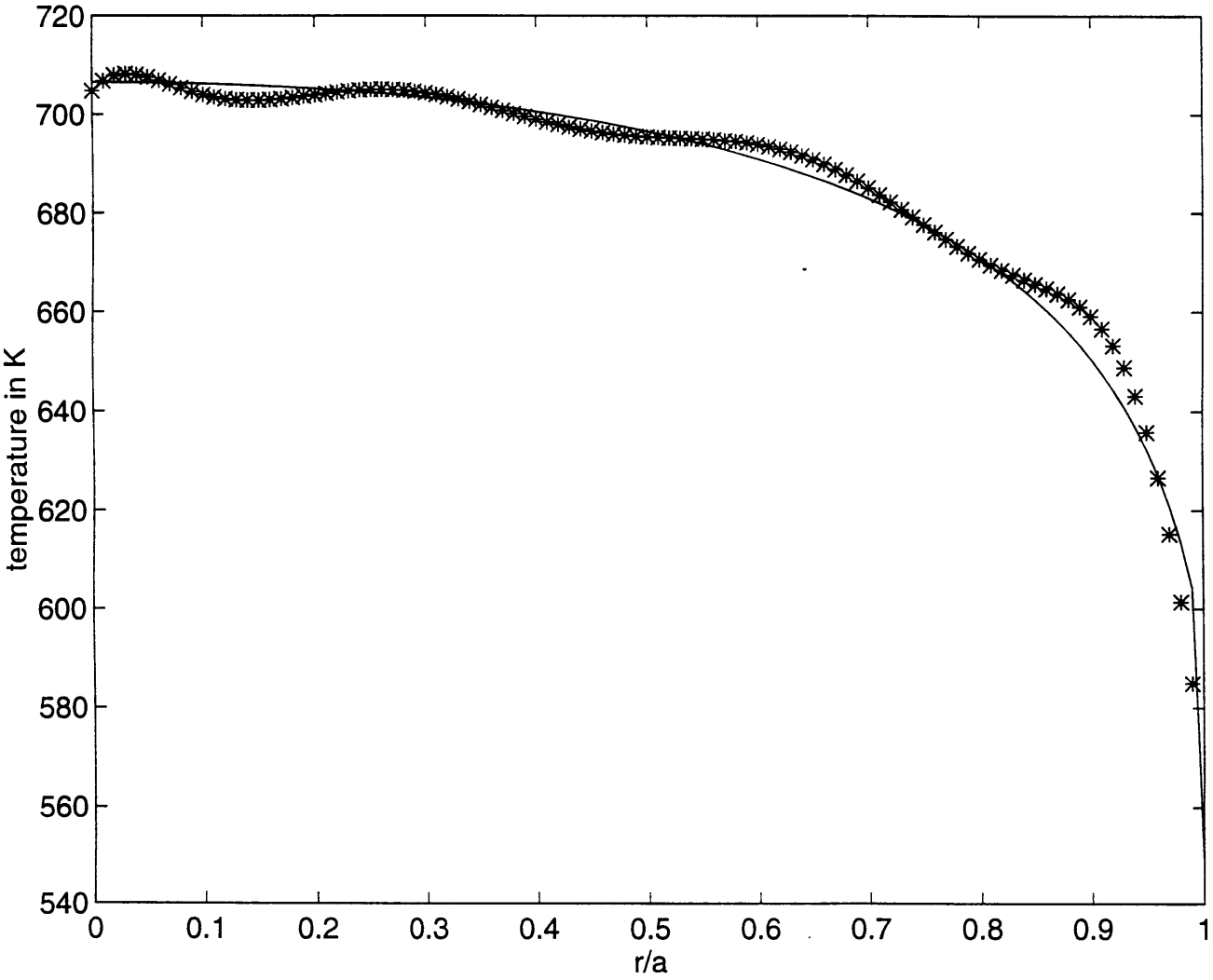
720
700
680
660
640
620
600
580
560
540
temperature in K
0
0.1
0.2
0.3
0.4
0.5
0.6
0.7
0.8
0.9
1
r/a

Figure 6.

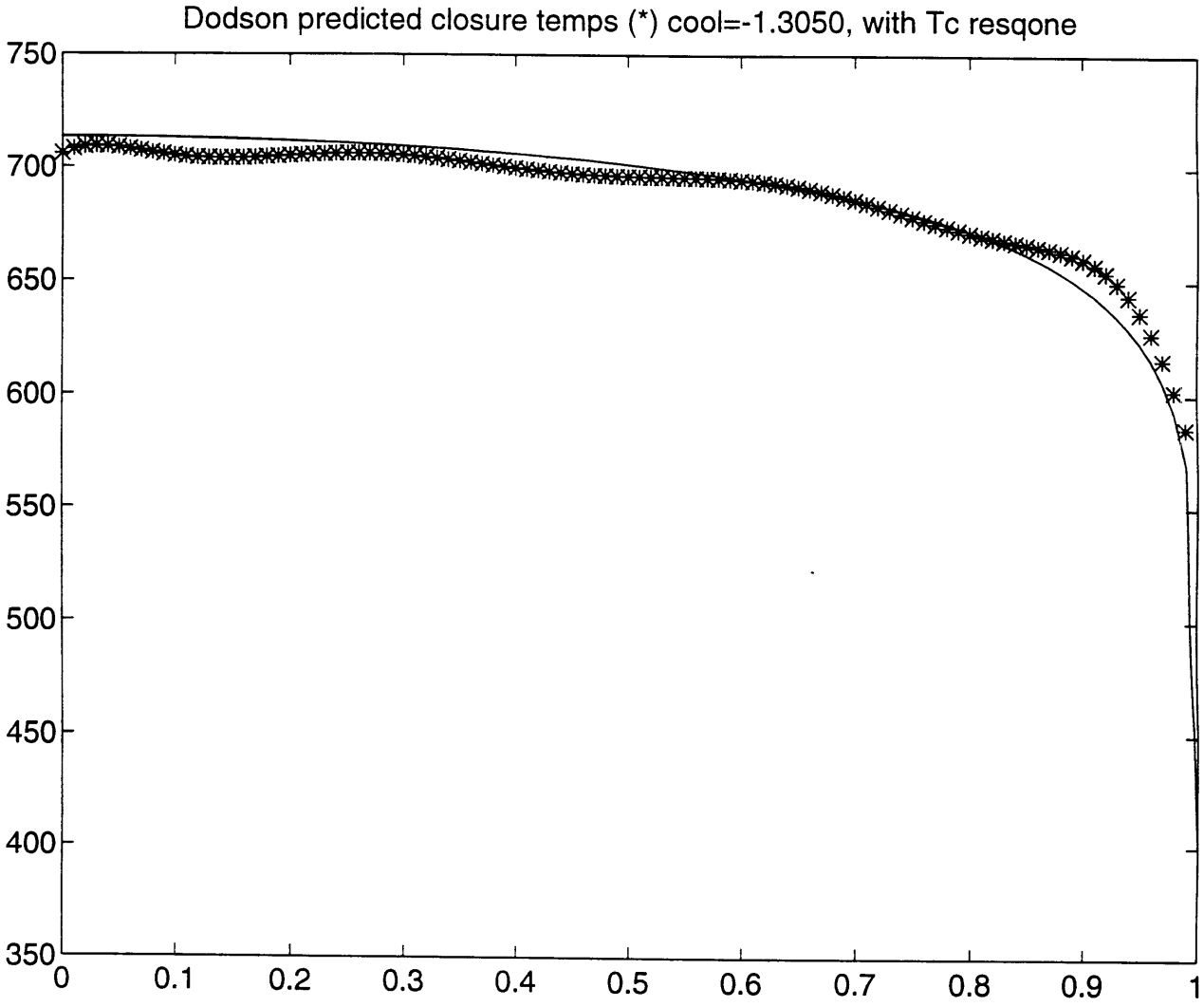
Dodson predicted closure temps (*) cool=-1.3050, with Tc resqone
750
700
650
600
550
500
450
400
350
0
0.1
0.2
0.3
0.4
0.5
0.6
0.7
0.8
0.9
1

Figure 7.

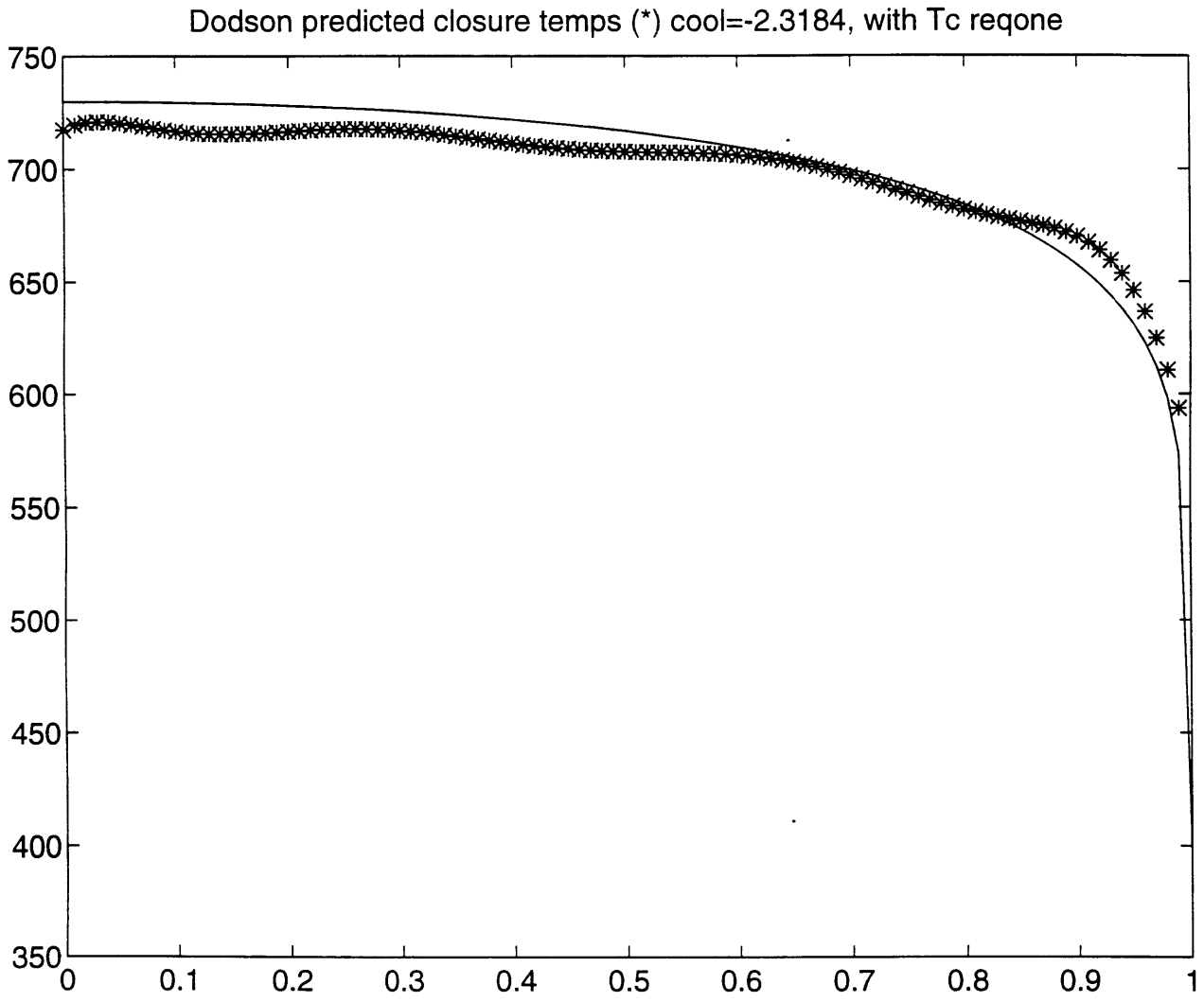
Dodson predicted closure temps (*) cool=-2.3184, with Tc reqone
750
700
650
600
550
500
450
400
350
0
0.1
0.2
0.3
0.4
0.5
0.6
0.7
0.8
0.9
1

Figure 8.

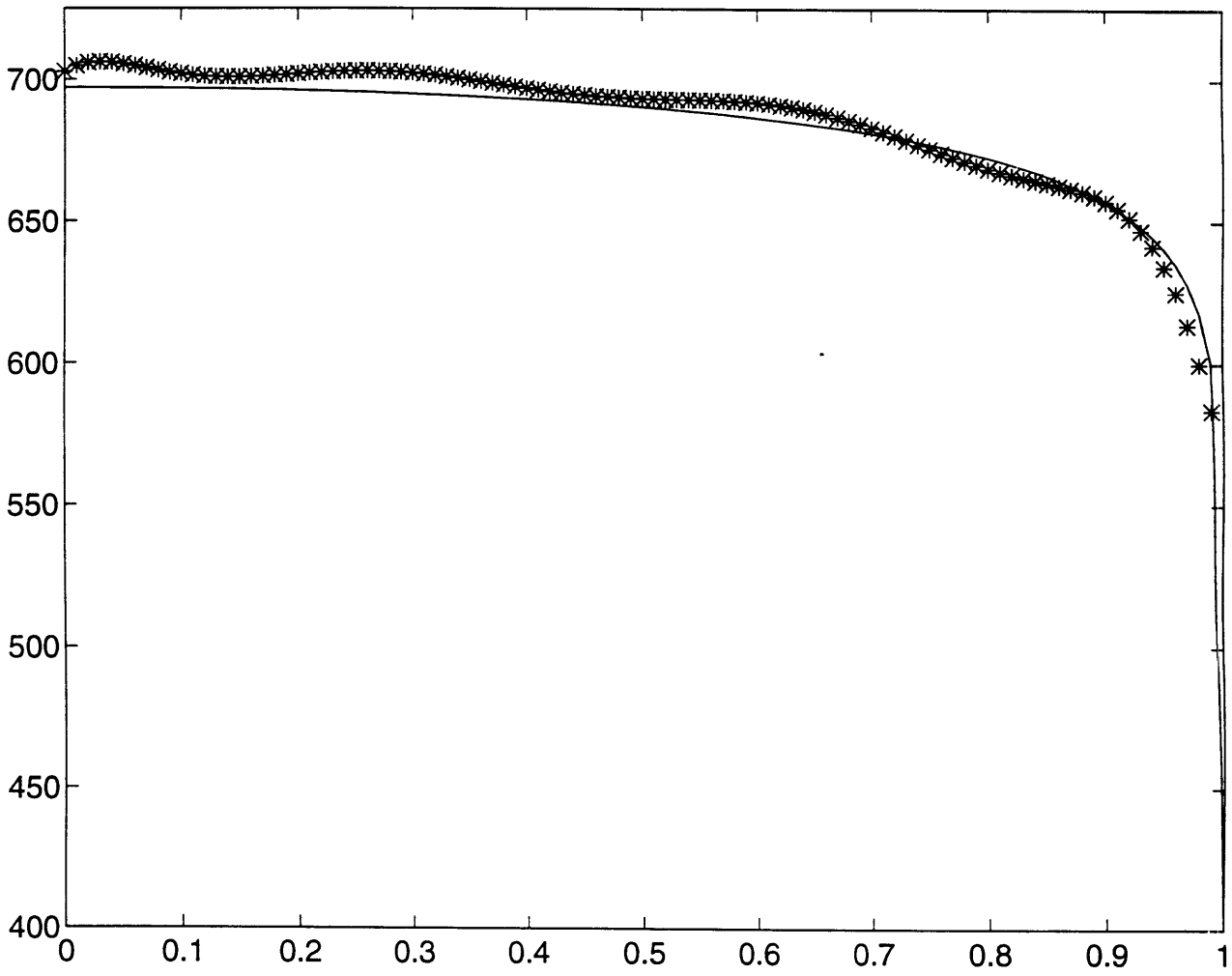

Figure 9.

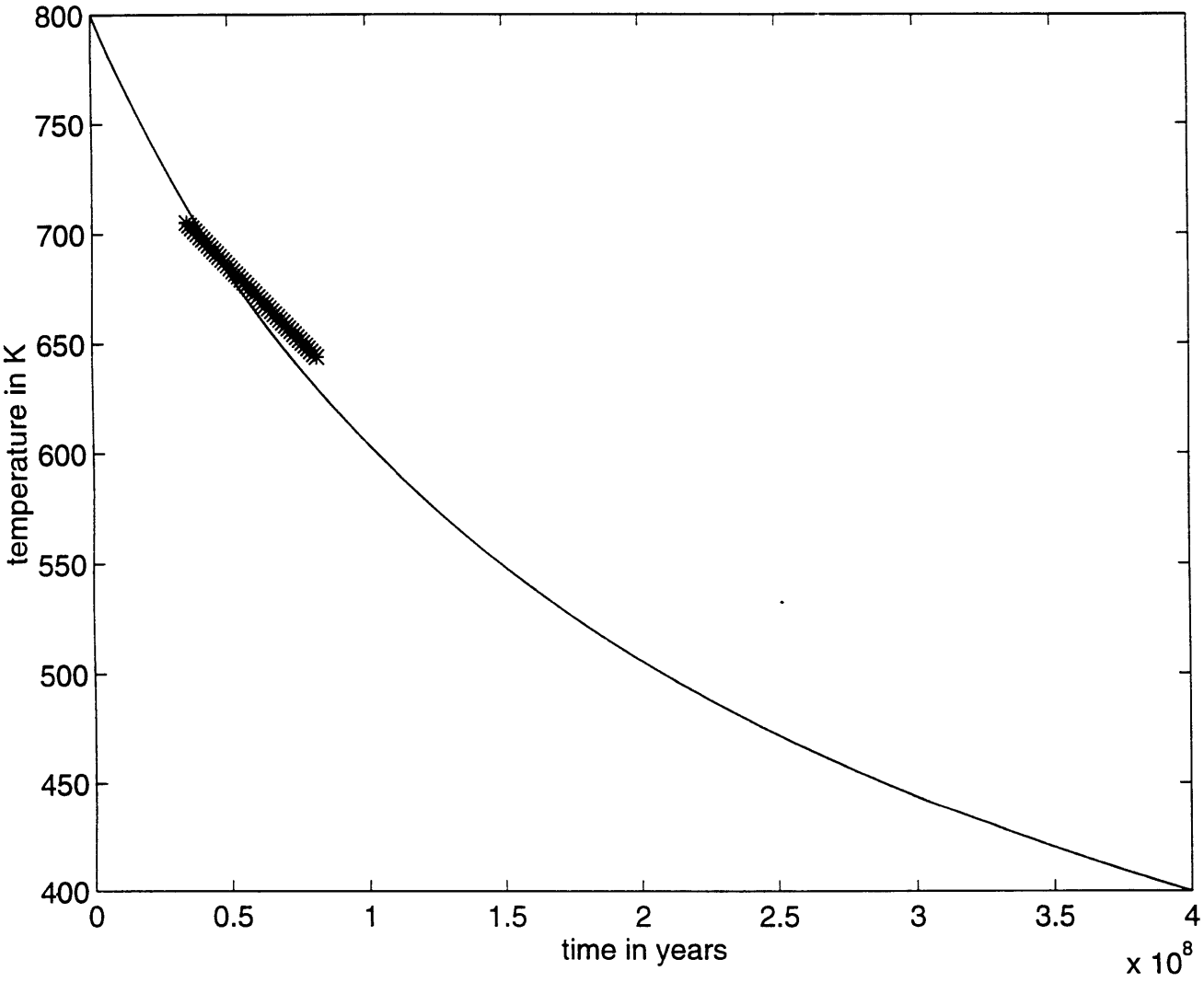
800
750
700
650
600
550
500
450
400
temperature in K
0
0.5
1
1.5
2
2.5
3
3.5
4
time in years
x 10^8

Figure 10.

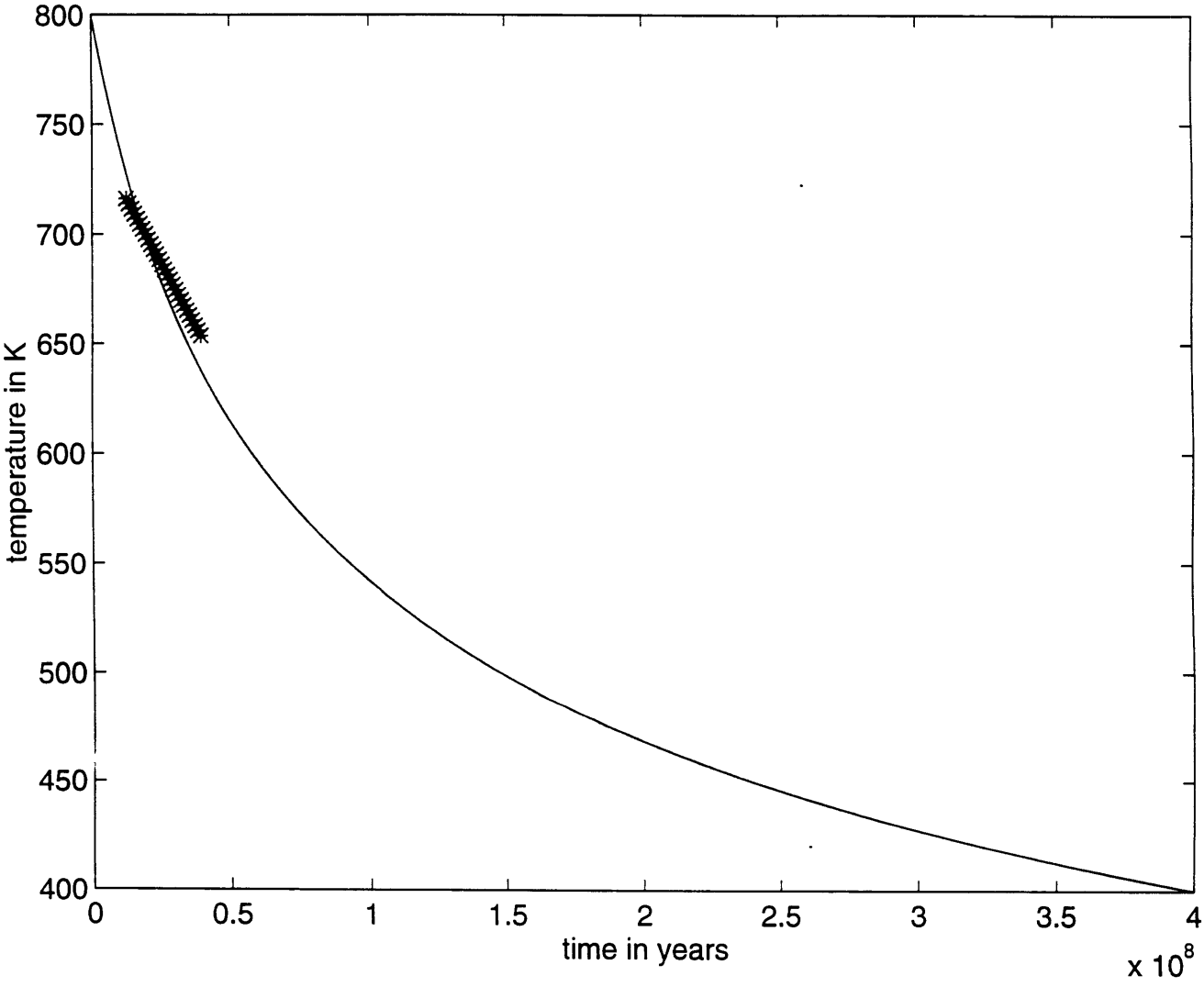
800
750
700
650
600
550
500
450
400
temperature in K
0
0.5
1
1.5
2
2.5
3
3.5
4
time in years
x 10^8

Figure 11.

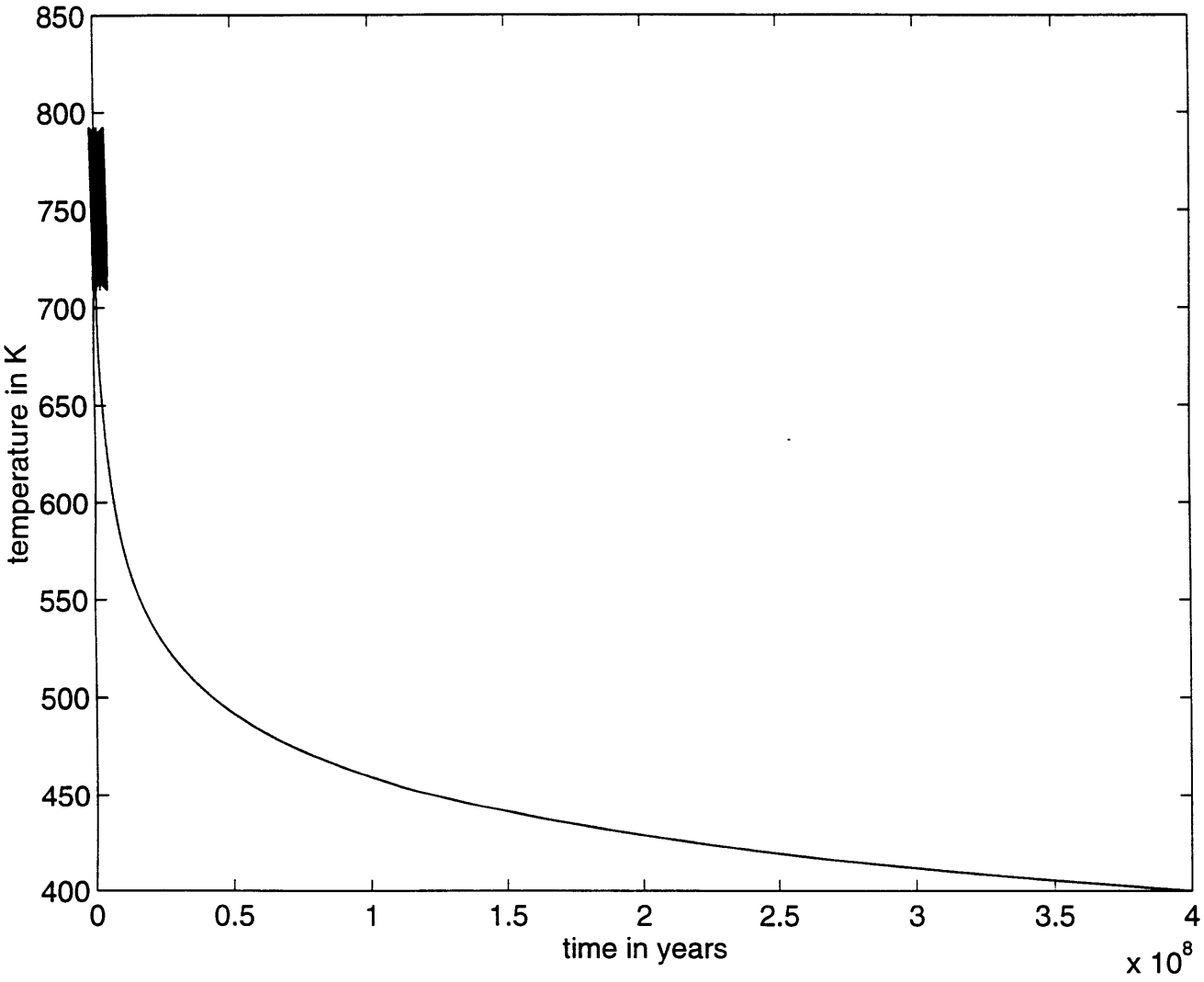
850
800
750
700
650
600
550
500
450
400
temperature in K
0
0.5
1
1.5
2
2.5
3
3.5
4
time in years
x 10^8

Figure 12.

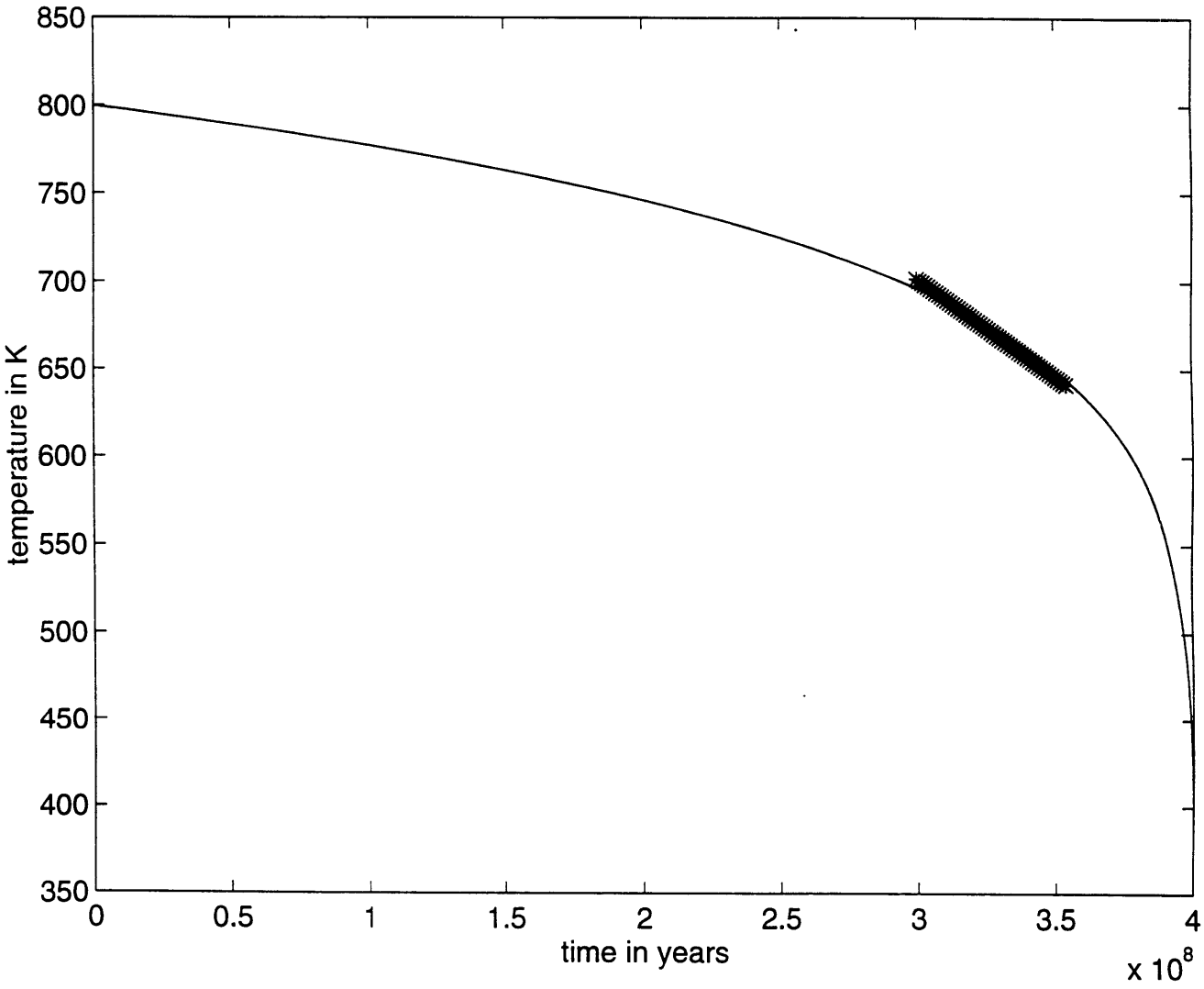
850
800
750
700
650
600
550
500
450
400
350
temperature in K
0
0.5
1
1.5
2
2.5
3
3.5
4
time in years
x 10^8

Figure 13.

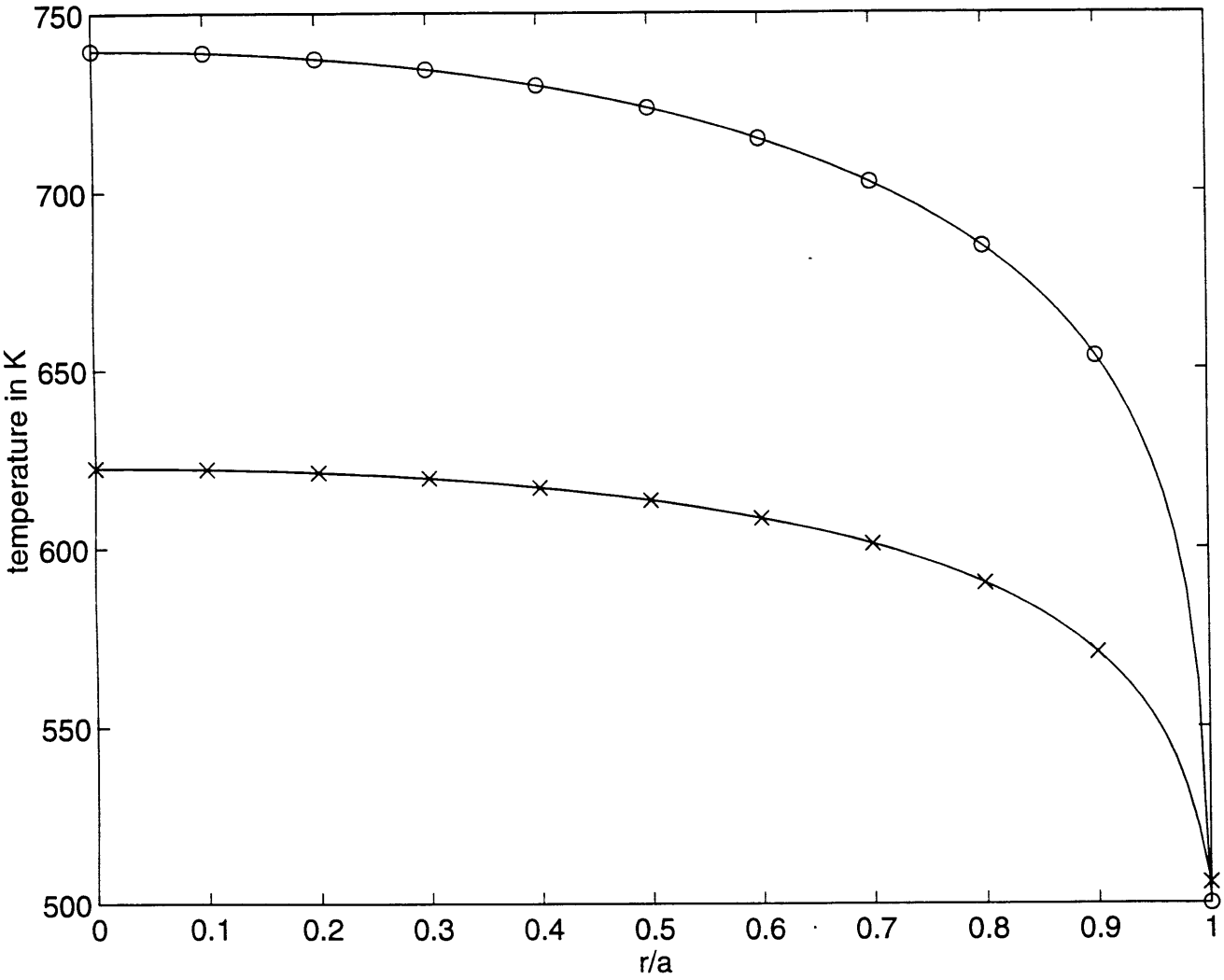
750
700
650
600
550
500
temperature in K
0
0.1
0.2
0.3
0.4
0.5
0.6
0.7
0.8
0.9
1
r/a

Figure 14.

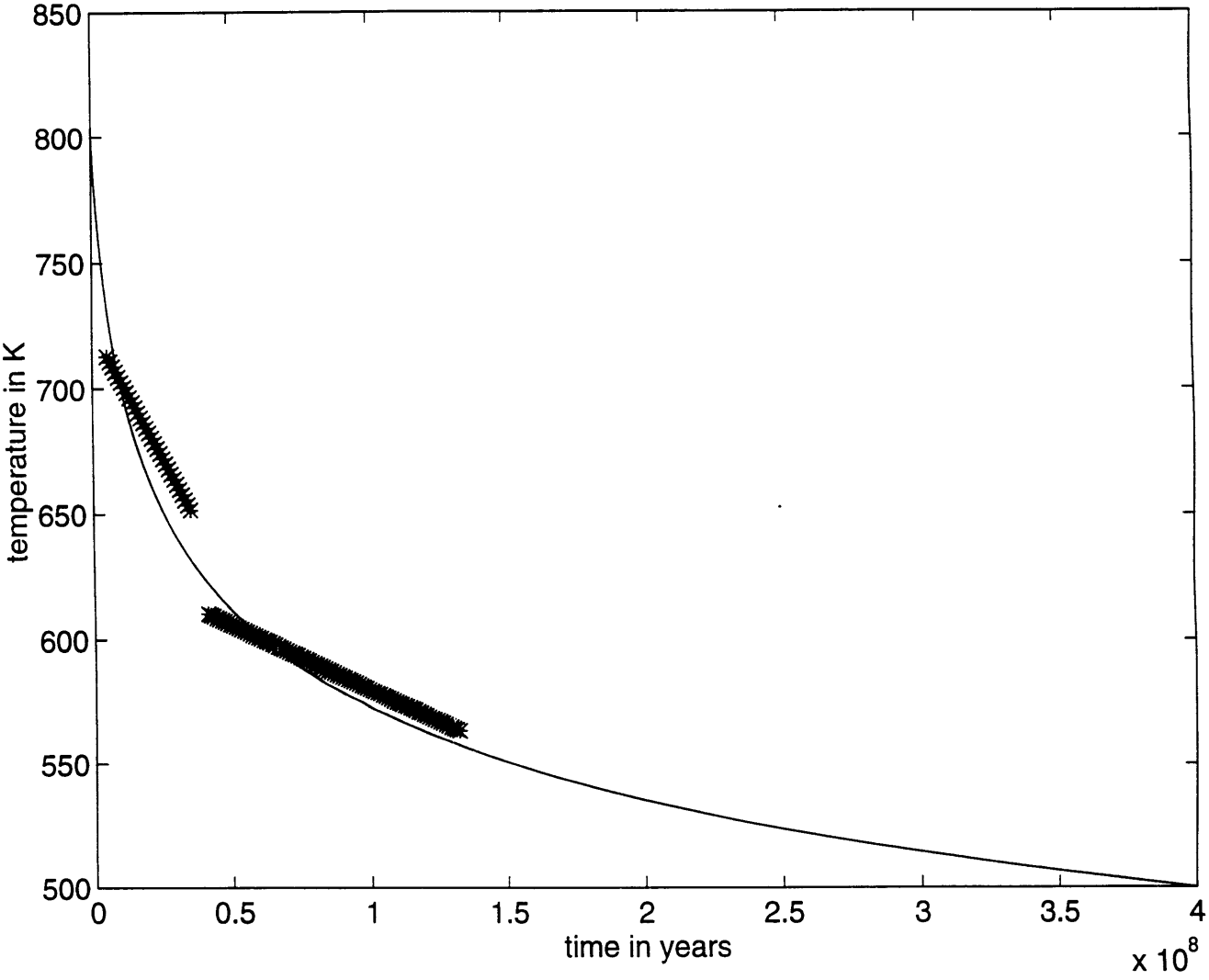
850
800
750
700
650
600
550
500
temperature in K
0
0.5
1
1.5
2
2.5
3
3.5
4
time in years
x 10^8

Figure 15.

Map of New Mexico

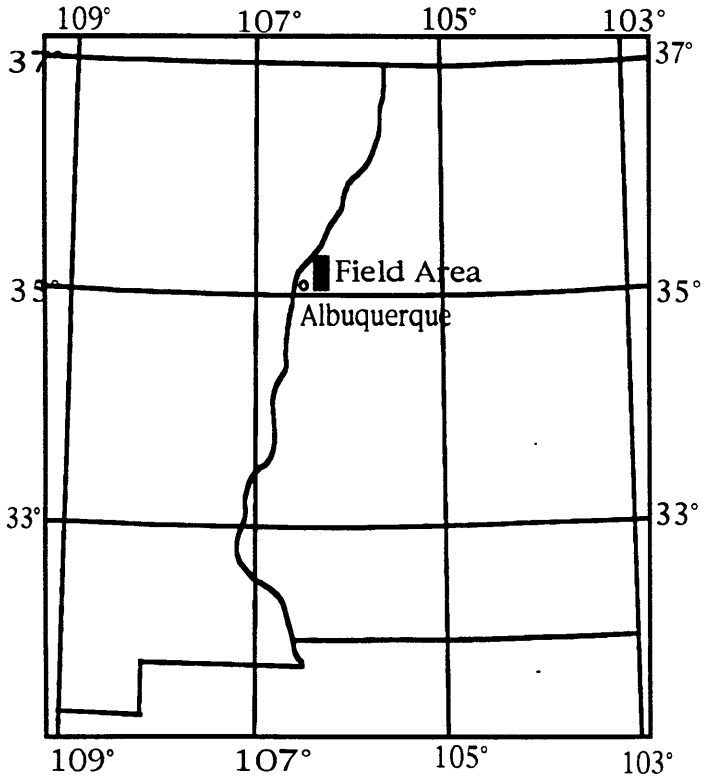

Figure 16.

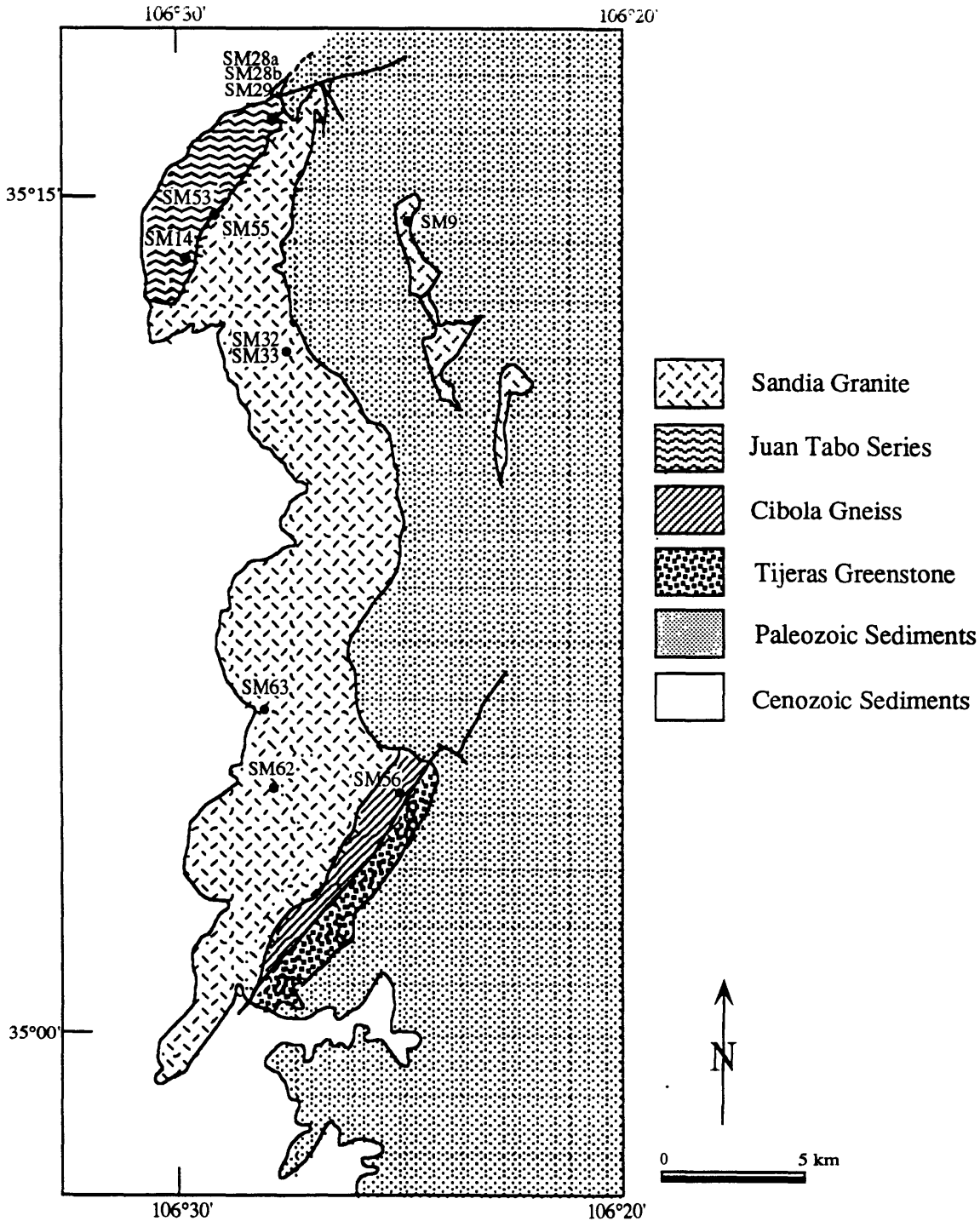
106°30'
106°20'
35°15'
35°00'
SM28a
SM28b
SM29
SM53
SM55
SM14
SM9
SM32
SM33
SM63
SM62
SM56
Sandia Granite
Juan Tabo Series
Cibola Gneiss
Tijeras Greenstone
Paleozoic Sediments
Cenozoic Sediments
N
0
5 km

Figure 17.

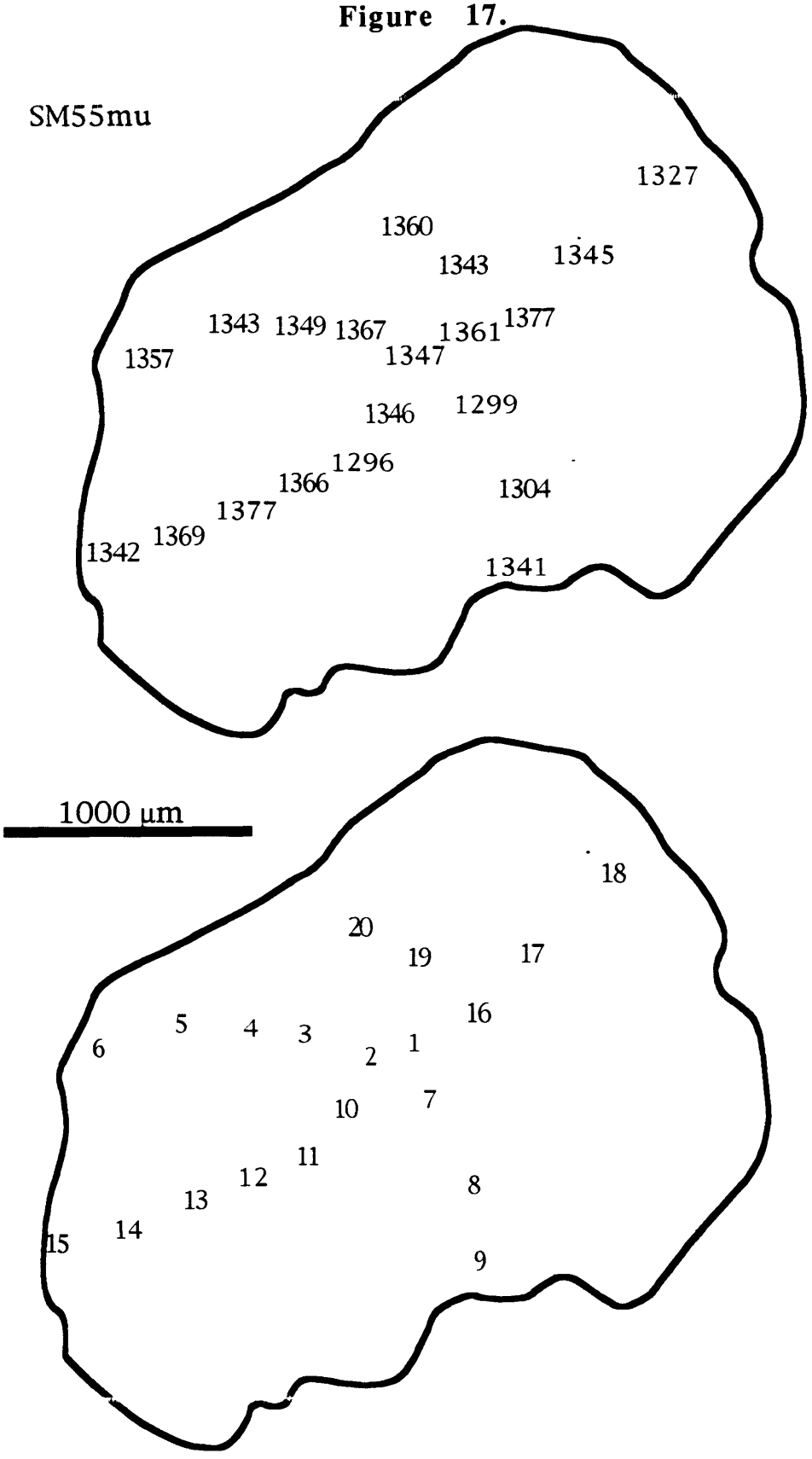
SM55mu
1327
1360
1343
1345
1343
1349
1367
1361
1377
1357
1347
1346
1299
1296
1366
1304
1377
1369
1342
1341
1000 µm
18
20
19
17
16
5
4
3
6
2
1
7
10
11
12
8
13
14
15
9

Figure 18.
SM32mu

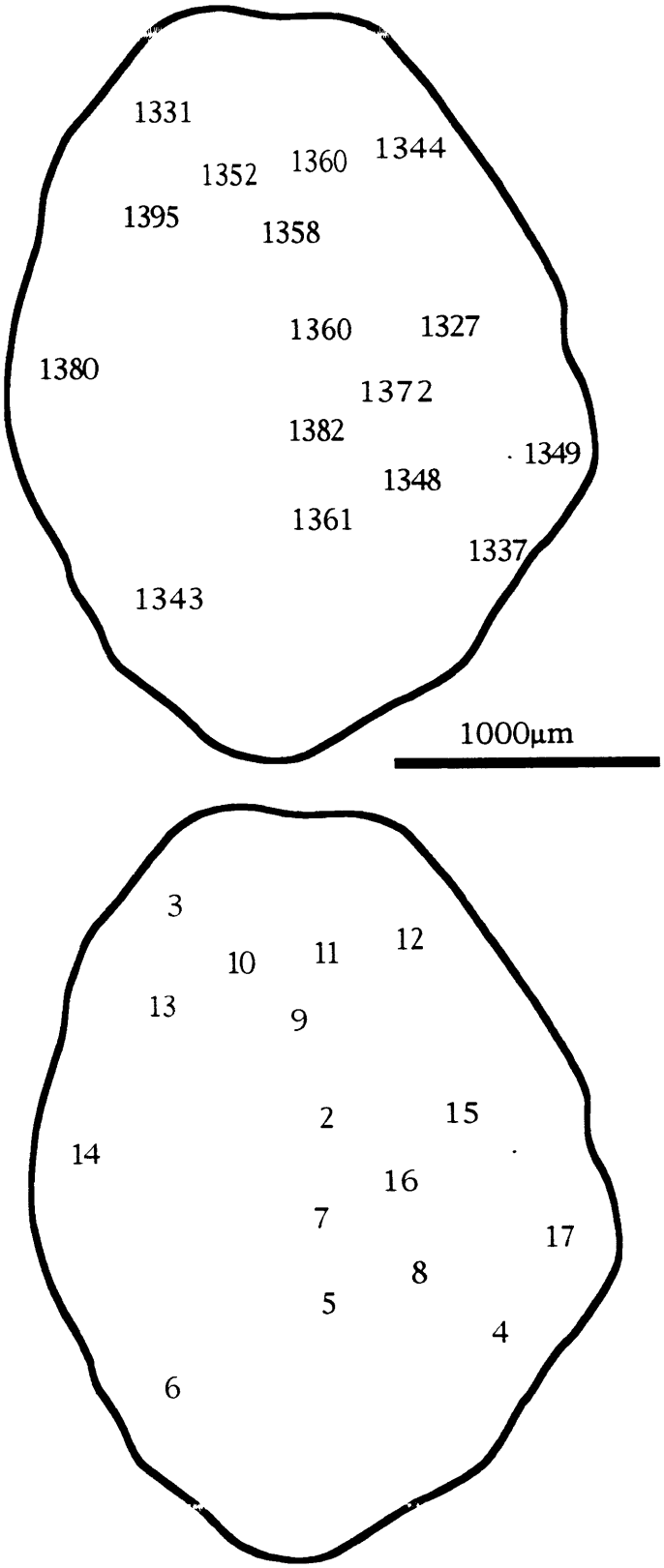

Figure 19.

SM33bt

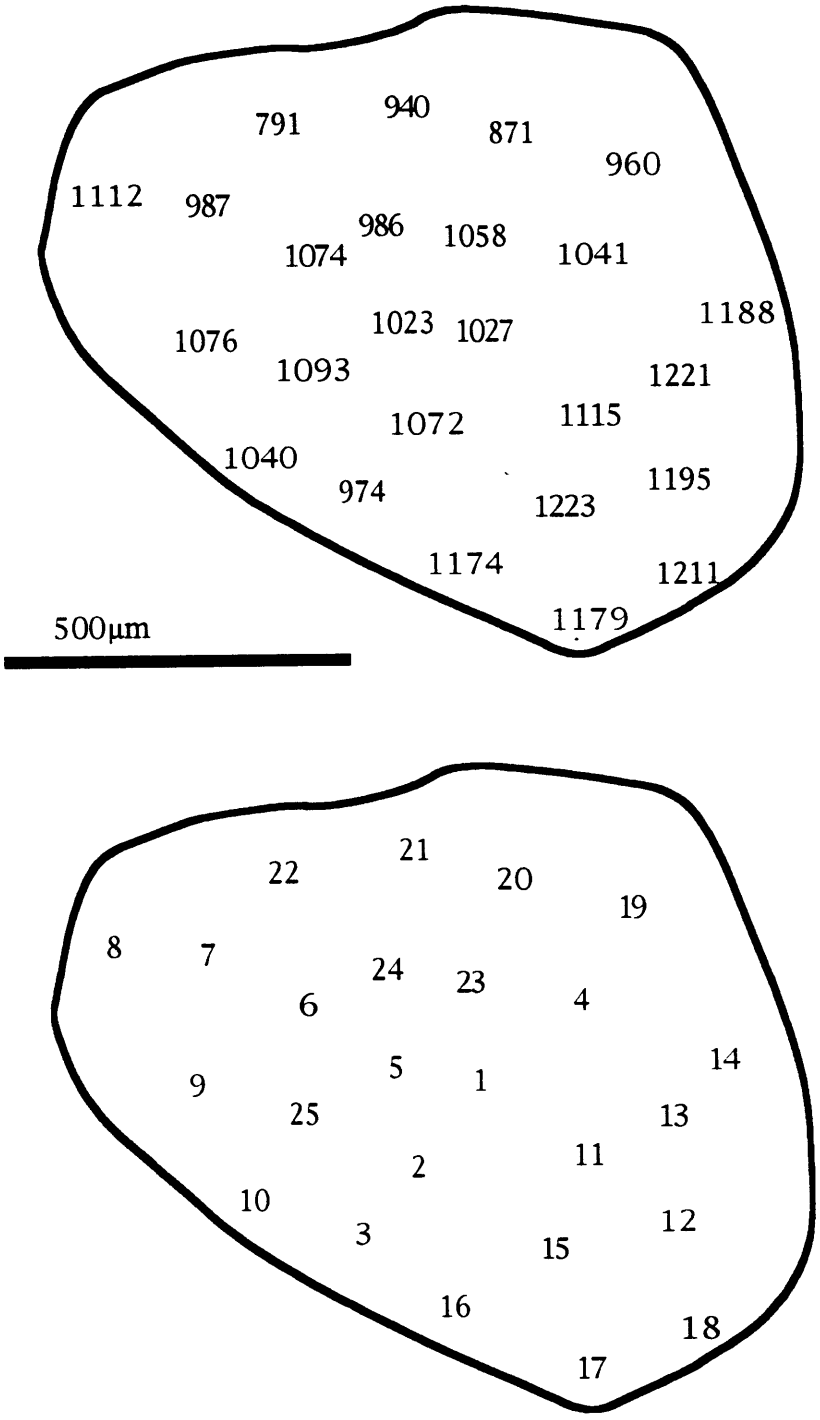

Figure 20.

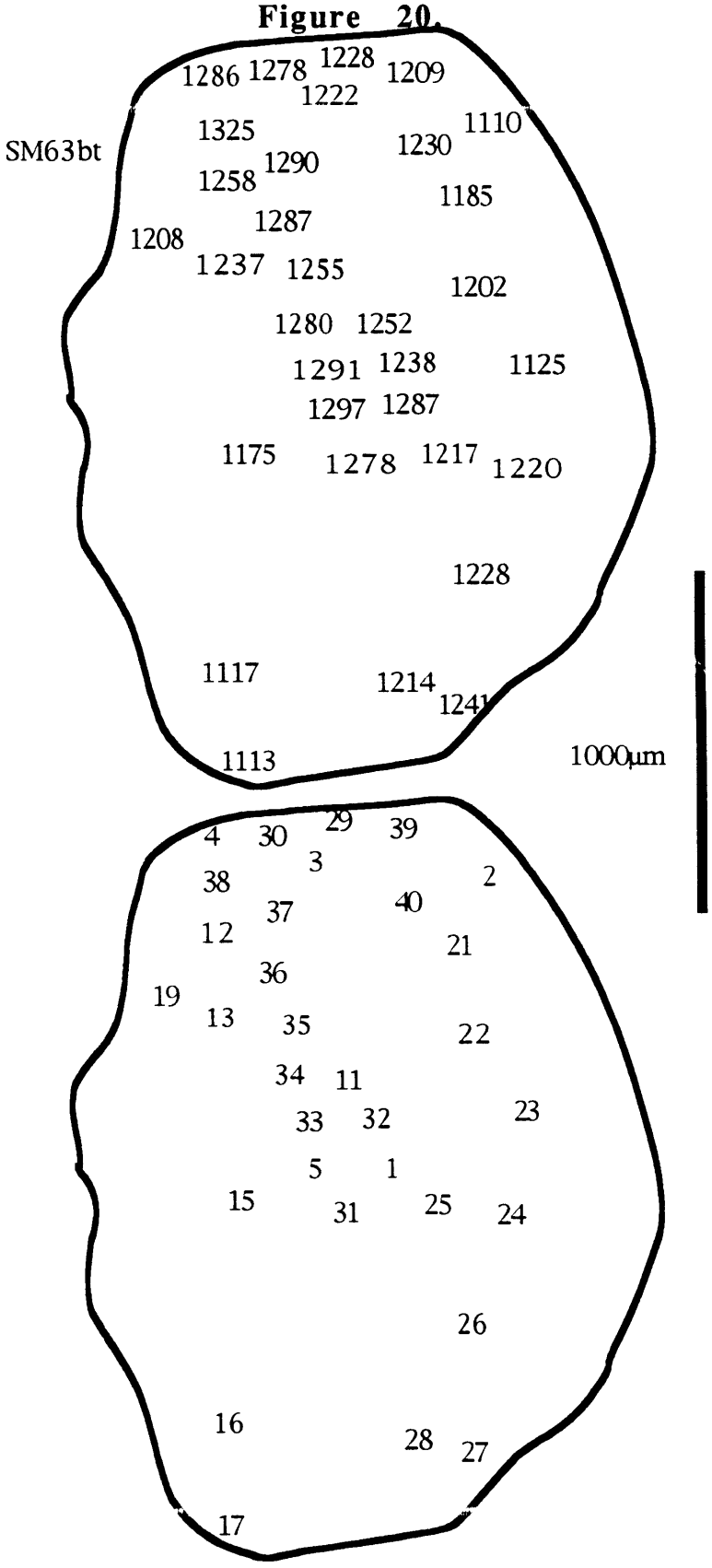
SM63bt
1286
1278
1228
1209
1222
1325
1110
1230
1290
1258
1185
1287
1208
1237
1255
1202
1280
1252
1291
1238
1125
1297
1287
1175
1278
1217
1220
1228
1117
1214
1241
1113
1000µm
4
30
29
39
3
38
2
40
37
12
21
36
19
13
35
22
34
11
33
32
23
5
1
15
31
25
24
26
16
28
27
17

Figure 21.

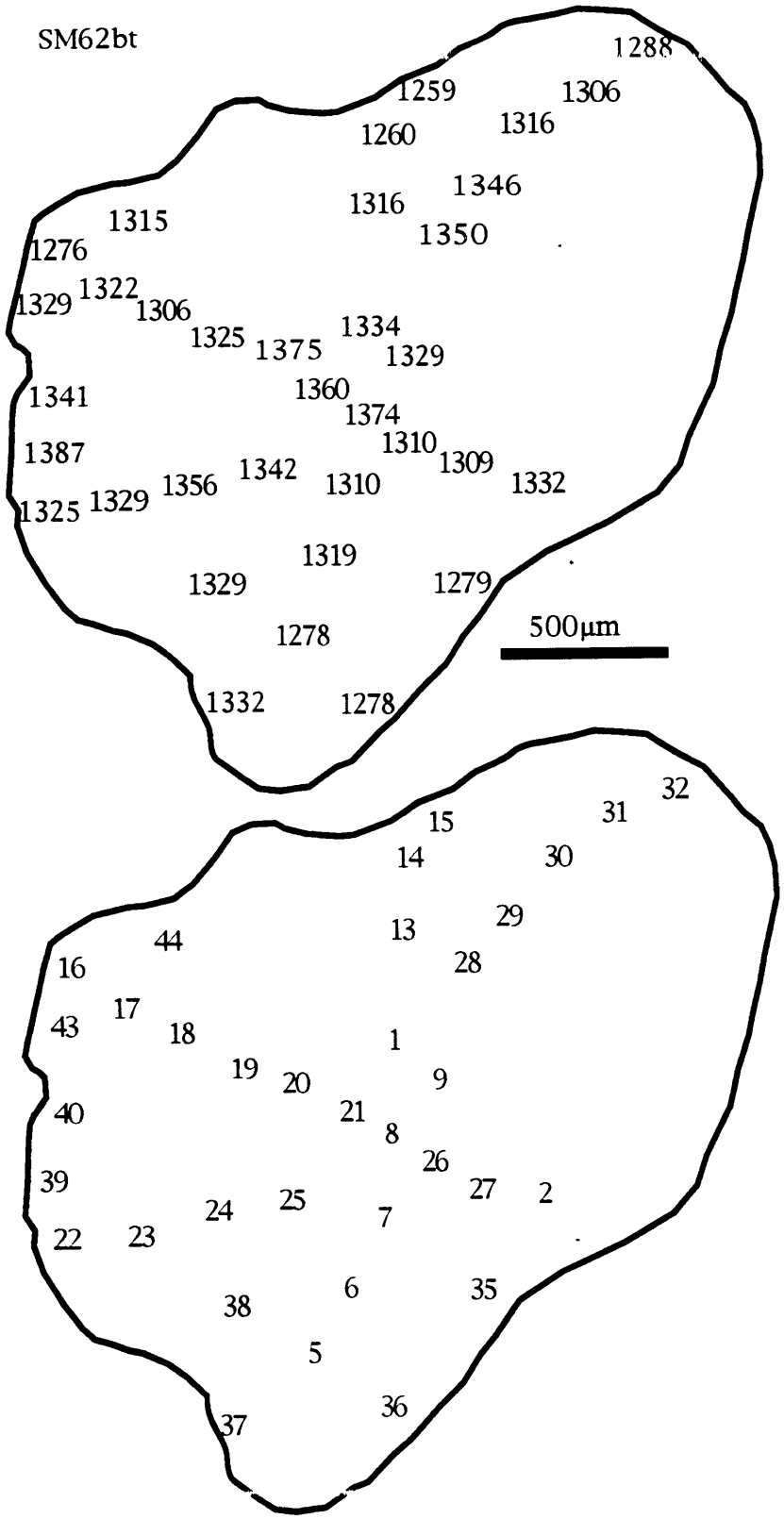
SM62bt
1288
1259
1306
1316
1260
1346
1316
1315
1350
1276
1329
1322
1306
1325
1375
1334
1329
1341
1360
1374
1310
1387
1342
1309
1356
1310
1332
1325
1329
1319
1329
1279
1278
500µm
1332
1278
32
31
15
14
30
29
13
44
28
16
17
43
18
1
19
20
9
40
21
8
26
39
27
2
24
25
7
22
23
6
35
38
5
36
37

Figure 22.

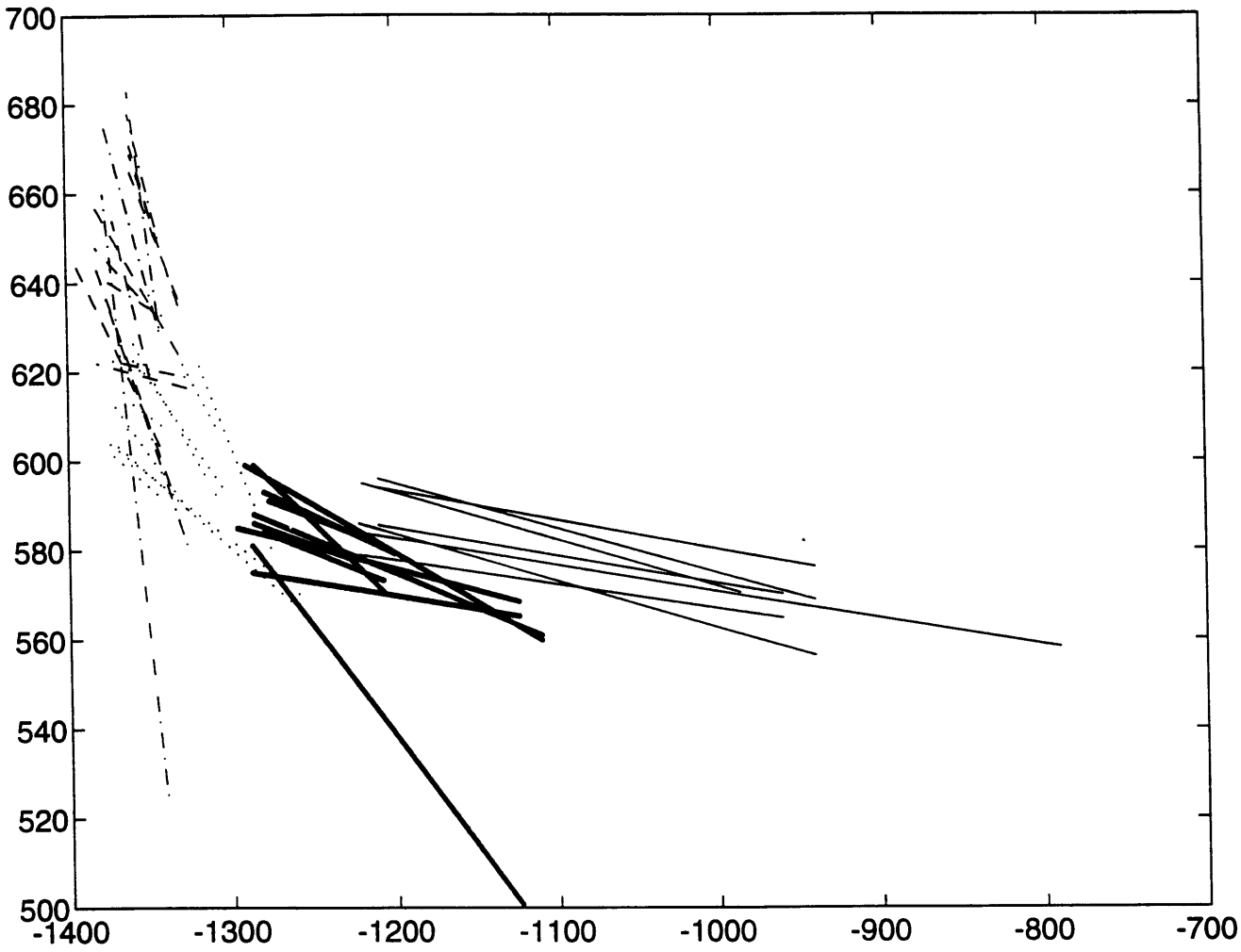

2808-11